# Tumor microenvironments impair T cell receptor affinity and function

Zhou Yuan[1,2†a], Meghan J. O'Melia[3†b], Kaitao Li[2,3], Jintian Lyu[2,3], Fangyuan Zhou[1,2,3c], Prithiviraj Jothikumar[2,3d], Nathan A. Rohner[1,2], Margaret P. Manspeaker[2,4], David M. Francis[2,4], Ke Bai[2,3e], Chenghao Ge[2,3f], Muaz N. Rushdi[2,3g], Loice Chingozha[2,4h], Samuel Ruipérez-Campillo[2,3i], Hang Lu[2,4], Susan N. Thomas[1,2,3,5*], Cheng Zhu[1,2,3,5*]

[1]George W. Woodruff School of Mechanical Engineering, Georgia Institute of Technology

[2]Parker H. Petit Institute for Bioengineering and Bioscience, Georgia Institute of Technology

[3]Wallace H. Coulter Department of Biomedical Engineering, Georgia Institute of Technology and Emory University

[4]School of Chemical and Biomolecular Engineering, Georgia Institute of Technology

[5]Winship Cancer Institute, Emory University

[†]These authors contributed equally to this work.

*To whom correspondence should be addressed: susan.thomas@gatech.edu and cheng.zhu@bme.gatech.edu

[a]Present address: Department of Bioengineering, University of California, San Diego, La Jolla, CA 92093
[b]Present address: Department of Radiation Oncology, Harvard Medical School, Massachusetts General Hospital, Boston, MA 02114
[c]Present address: Microfabrica Inc., 7911 Haskell Ave, Van Nuys, CA 91406
[d]Present address: Amazon Web Services, 3333 Piedmont Rd NE, Atlanta, GA 30305
[e]Present address: National Institute on Deafness and Other Communication Disorders, National Institutes of Health, Bethesda, MD 20814
[f]Present address: Amgen Inc., One Amgen Center Dr., Thousand Oaks, CA 91320
[g]Present address: Medtronic CO., Minneapolis, MN, USA
[h]Present address: Intel Corporation, 2501 NE Century Blvd, Hillsboro, OR 97124
[i]Present address: Department of Information Technology and Electrical Engineering, Swiss Federal Institute of Technology (ETH) Zürich, Zürich, Switzerland; School of Medicine, Stanford University, Palo Alto, CA, USA

## Abstract

$CD8^+$ T cells underpin effective anti-tumor immune responses in melanoma; however, their functions are attenuated due to various immunosuppressive factors in the tumor microenvironment (TME), resulting in disease progression. T cell function is elicited by the T cell receptor (TCR), which recognizes antigen peptide-major histocompatibility complex (pMHC) expressed on tumor cells via direct physical contact, i.e., two-dimensional (2D) interaction. TCR–pMHC 2D affinity plays a central role in antigen recognition and discrimination, and is sensitive to both the conditions of the T cell and the microenvironment in which it resides. Herein, we demonstrate that $CD8^+$ T cells residing in TME have lower 2D TCR–pMHC bimolecular affinity and TCR–pMHC–CD8 trimolecular avidity, pull fewer TCR–pMHC bonds by endogenous forces, flux lower level of intracellular calcium in response to antigen stimulation, exhibit impaired *in vivo* activation, and show diminished anti-tumor effector function. These detrimental effects are localized in the tumor and tumor draining lymph node (TdLN), and affect both antigen-inexperienced and antigen-experienced $CD8^+$ T cells irrespective of their TCR specificities. These findings implicate impaired antigen recognition as a mechanism of T cell dysfunction in the TME.

48 **Introduction**

49 Spontaneous development of $CD8^+$ T cell immunity against melanomas is associated with
50 improved clinical outcomes (*1, 2*). Immunotherapy therefore has a high potential for the treatment
51 of advanced melanoma, which is among the common cancer types with poor clinical outcomes at
52 advanced disease stages (*3*). The protective effects of effector $CD8^+$ T cells are often inhibited
53 within the tumor microenvironment (TME), however, resulting in unchecked tumor growth (*4-8*).
54 To this end, therapeutic immune checkpoint blockade (ICB) of programmed cell death 1 (PD-1)
55 signaling, thought to work both by expanding the pool of pre-existing stem-like $CD8^+$ T cells (*9*)
56 and reinvigorating exhausted tumor-infiltrating lymphocytes (TILs) from immune-suppression (*10,*
57 *11*), has emerged as a successful treatment that induces durable objective responses in 25-30% of
58 patients with advanced melanoma (*12, 13*). ICB therefore represents a highly promising therapy
59 class to address the high and increasing mortality associated with melanoma. However, the success
60 of ICB therapies relies on the existence of robust, pre-existing $CD8^+$ T cell immunity (*14, 15*).
61 Elucidating the mechanisms suppressing both the development and function of $CD8^+$ T cell anti-
62 tumor immunity against endogenously generated tumor neoantigens during disease progression or
63 through therapeutic vaccination can therefore help develop strategies to improve the success of
64 melanoma immunotherapy.

65 T cell anti-tumor immunity is initiated by antigen recognition of the T cell receptor (TCR)
66 via interaction with peptide-major histocompatibility complex (pMHC). TCR–pMHC affinity is
67 an important driver of $CD8^+$ T cell anti-tumor immunity, which is conventionally measured by the
68 surface plasmon resonance (SPR) technology using aglycosylated soluble proteins of TCR
69 ectodomain produced by *E. coli* or pMHC-tetramer staining of T cells (*16*). However, *in vivo* TCR–

70 pMHC interaction requires direct physical contact between the T cell and the tumor cell as the two
71 molecules reside on the respective cell surfaces and interact across the junctional gap between the
72 two opposing cell membranes.

73 We (*17-22*) and others (*23*) have shown that TCR–pMHC binding affinity measured *in situ*
74 at the T cell surface better correlates with T cell function. Such a measurement is termed two-
75 dimensional (2D) affinity because it has a unit of area, in contrast to the 3D affinity measured by
76 SPR that has a unit of volume. Similar to 3D affinity whose value may depend on pH or chemical
77 composition of the medium, the value of 2D affinity can be regulated by pharmacological
78 perturbations of the cellular environment *in vitro* (*17, 24*). Importantly, *ex vivo* measurements
79 found differential 2D affinities of monoclonal TCR on membranes of T cells isolated from splenic
80 red pulp vs white pulp, which are well correlated with differential transcriptomic changes,
81 differential effector functions, and differential developmental fates of these cells *in vivo* (*25*).
82 Remarkably, it was found that 2D affinity correlated with these phenotypes even in the cases where
83 the surface markers for cell subsets did not (*25*), highlighting the predictive power of our 2D
84 affinity measurement.

85 Using the B16F10 melanoma model most widely used for the preclinical investigation of
86 immunotherapeutic resistance, we reveal that the 2D affinity for and spontaneous pulling of TCR
87 on its cognate pMHC by $CD8^+$ T cells is impaired by the TME in which the T cells reside, and that
88 the lowered 2D TCR–pMHC affinity predicts suppressed effector functions. These findings
89 suggest altered TCR antigen recognition as a mechanism of immune evasion in melanoma,
90 independent of the inhibitory effects of immune checkpoint receptors, whose consideration may
91 help develop diagnostic and immunotherapeutic approaches to manage advanced disease.

92 **Results**

93 **TME suppresses antigen-induced expansion and function of CD8$^+$ T cells *in vivo***

94 The influence of the TME on CD8$^+$ T cell immunity was explored using a murine tumor model
95 (Fig. 1A) and a synthetic antigen system in which lymph-draining nanoparticles (NPs, Fig. 1B)
96 were disulfide-linked to the H2-K$^b$ presented immunodominant peptide of ovalbumin (OVA) with
97 a C-terminal cysteine, CSIINFEKL , (CSIINFEKL-NP or Ag-NP, Fig. 1C) that result in dose-
98 dependent cross-presentation in *in vitro* splenocyte cultures (Fig. 1D) (*26*). In this model, C57BL/6
99 mice were implanted in the lateral dorsal skin with a primary B16F10 melanoma at day (d) -8 (Fig.
100 1A, left). At d-1 (7 days post primary tumor implantation), Ag-NPs were administered
101 intratumorally (i.t.) into the primary B16F10 melanoma (Tumor-bearing) (Fig. 1A, left).
102 Alternatively, Ag-NPs were administered into the skin of tumor-naïve animals (Naïve) (Fig. 1A,
103 right) at d-1. In both schema (Fig. 1A), mice were implanted with OVA-expressing B16F10
104 (B16F10-OVA) melanoma cells at d0 (one day post Ag-NP administration) in either the dorsal
105 skin contralateral to the B16F10 melanoma or naïve skin contralateral to the Ag-NP injection site
106 in mice of the Tumor-bearing and Naïve cohorts, respectively. At d2, the Ag-NP injection site (the
107 primary B16F10 melanoma for the Tumor-bearing animals or skin for the Naïve animals) was
108 resected. In so doing, we could compare the influences on the growth of the OVA-expressing
109 secondary tumor and animal survival by the microenvironment in which the anti-OVA immunity
110 had been elicited by Ag-NP administration into naïve skin vs the primary tumor. As Ag-NPs result
111 in priming of CD8$^+$ T cells both at the local injection site as well as its draining lymph nodes (dLNs)
112 (*26*) due to these NPs unique lymph-draining behaviors (*27-32*), this system allowed us to compare
113 microenvironmental effects on CD8$^+$ T cells exerted both locally at the site of injection and within

114 lymph nodes (LNs) draining the naïve skin vs tumor after synthetic antigen administration without
115 animals succumbing to the primary tumor. Control of the B16F10-OVA secondary melanoma was
116 found to be less effective when Ag-NP treatment was administered into the primary B16F10
117 melanoma of the tumor-bearing animals compared to the skin of tumor-naïve animals, reflected in
118 both larger tumor volumes 14 days post injection (Fig. 1E) and shortened survival (Fig. 1F). These
119 data indicate that endogenous $CD8^+$ T cells primed by Ag-NP within the TME elicit less effective
120 anti-tumor responses than those primed by Ag-NP administration in the tumor-free (naïve) skin.

121 To further test the above contention, we compared the effects of the melanoma TME on
122 the antigen-specific activation and expansion of carboxyfluorescien succinimidyl ester (CFSE)
123 labelled $CD8^+$ OT-I T cells transferred to C57BL/6 animals in response to the OVA antigen
124 delivered by Ag-NP (Fig. 1G). Tumor-bearing $CD45.1^+$ recipient mice were implanted with
125 B16F10 melanomas at d-7, received adoptive transfer of $CD8^+$ T cells isolated from $CD45.2^+$ OT-
126 I donor mice at d-1, were injected i.t. with either Ag-NPs or saline on d0, and were sacrificed at
127 d3 to recover the donor $CD8^+$ T cells to measure their quantity and quality (Fig. 1G, left). For
128 comparison, donor $CD8^+$ T cells were likewise assessed after recovered from tumor-naïve $CD45.1^+$
129 recipient mice (comprising the Naïve cohort) that received adoptive transfer of $CD8^+$ T cells
130 isolated from $CD45.2^+$ OT-I donor mice d-1, were intradermally (i.d.) administered Ag-NPs or
131 saline one day later (d0), and were sacrificed at d3 (three days post injection of Ag-NP) (Fig. 1G,
132 right). No statistically significant differences in the overall extent of proliferation by donor $CD8^+$
133 T cells localized within the tissue site of injection were seen between the Tumor-bearing and -
134 Naïve groups challenged with Ag-NP (Fig. 1H), in line with reports that antigenic priming induces
135 a programmed proliferation response in $CD8^+$ T cells (*33*). The frequency and relative number of
136 donor $CD8^+$ T cells expressing PD-1, which was increased upon recent antigen experience or

137 chronic antigen stimulation (*34*), was similar in Tumor-bearing and -Naïve recipient animals in
138 response to Ag-NP challenge (Fig. 1I-J). However, the frequency of $CD8^+$ donor cells expressing
139 the activation marker CD25 in response to Ag-NP treatment was significantly lower in tumors of
140 Tumor-bearing animals than the naïve skin injection site of Naïve animals (Fig. 1I). To account
141 for differences in lymphocyte homing to tumors vs skin (*35*), the overall numbers of donor $CD8^+$
142 T cells in tumors of Tumor-bearing animals and skin of Naïve animals were respectively
143 normalized to those measured in animals from each group that had been challenged with saline
144 instead of Ag-NPs. With this method that accounts for intrinsic microenvironmental differences in
145 total levels of lymphocyte accumulation in the tissue site of analysis, CD25-expressing donor
146 $CD8^+$ T cell numbers that resulted specifically from Ag-NP challenge were found to increase in
147 the skin of saline injected Naïve animals but not in tumors of Tumor-bearing animals. Ag-NP
148 challenge likewise increased the number of $CD44^-$ donor cells in tumors of Tumor-bearing animals
149 relative to the skin of Naïve animals (Fig. 1J). These data indicate that the TME locally suppresses
150 overall levels of antigen-specific $CD8^+$ T cell activation in response to antigen challenge.

151 Given the known role of LNs draining the tumor (TdLNs) in mediating adaptive immunity
152 and response to therapy (*26, 36, 37*), responses to Ag challenge of donor $CD8^+$ T cells recovered
153 from TdLNs of Tumor-bearing animals were compared to those from LNs draining the Ag-NP-
154 injected skin of Naïve animals. The total numbers of PD-1- and CD25-expressing donor $CD8^+$ T
155 cells were significantly lower in the TdLNs of Tumor-bearing animals than those draining the Ag-
156 NP injected skin of Naïve animals (Fig. 1K), in contrast to the lack of local changes within the
157 tumor of Tumor-bearing animals relative to the skin injection site of Naïve animals. Moreover,
158 PD-1 expression was significantly lower in donor $CD8^+$ T cells recovered from TdLNs of Tumor-
159 bearing animals intratumorally challenged with Ag-NPs than LNs draining the Ag-NP injected

160 skin of Naïve animals (Fig. 1L), an effect observed in both early and late proliferative generations
161 (Fig. 1M). However, statistically indistinguishable levels of PD-1 or CD25 were observed on
162 donor $CD8^+$ T cells recovered from spleens of Tumor-bearing and Naïve recipient animals after
163 Ag challenge (Fig. 1N). Collectively, these results demonstrate that $CD8^+$ T cells within the TME
164 and TdLNs, but not in spleen, exhibit less robust response to antigenic priming *in vivo*.

165 **Activation by and TCR binding to antigen pMHC is suppressed in $CD8^+$ T cells recovered**
166 **from TME and TdLNs**

167 The diminished responses of $CD8^+$ T cells to antigen priming within tumor and TdLNs
168 (collectively referred to as TME) were further explored using $CD45.1^+$ C57BL/6 mice that were
169 tumor naïve (Naïve) or had been implanted B16F10 melanoma (Tumor) at d-7, received adoptive
170 transfer of $CD45.2^+$ $CD8^+$ OT-I T cells at d0, and sacrificed at d3 to harvest donor cells from the
171 tumor, skin or dLNs (Fig. 2A). Donor $CD8^+$ T cells were stimulated *in vitro* with SIINFEKL, and
172 responses were measured by intracellular cytokine staining, finding lower frequency of activation
173 marker CD69-expressing cells harvested from the tumor than from the skin of naïve animals (Fig.
174 2B). Furthermore, a higher frequency of donor cells from the tumor than skin expressed tumor
175 necrosis factor (TNF) α, whereas similar frequencies of donor cells from the same two sites
176 expressed interferon (IFN) γ, interleukin (IL) 2, and granzyme (GzmB) (Fig. 2B). Moreover,
177 significantly lower frequency of donor $CD8^+$ T cells from TdLNs of Tumor-bearing animals than
178 skin-dLNs of Naïve animals expressed CD69 and PD-1, whereas similar frequencies of donor cells
179 from the same two sites expressed TNF-α, IFN-γ, IL-2, and GzmB (Fig. 2C). By comparison,
180 statistically indistinguishable numbers of donor $CD8^+$ T cells were found from the spleens of
181 tumor-bearing and -naive recipient mice that expressed CD69, PD-1, TNF-α, IFN-γ, IL-2, and

182 GzmB (Fig. 2D). These results corroborate data generated in response to *in vivo* antigen encounter
183 and show that microenvironmental factors derived from the tumor, which are present in TdLNs
184 but not spleens in this model (*37, 38*), suppresses $CD8^+$ T cell activation induced by antigen
185 recognition.

186 Antigen recognition is initiated by TCR–pMHC interaction that occurs at the cross-
187 junctional space spanning the gap between the membranes of the T cell and the tumor cell, i.e., 2D
188 binding, which could be regulated by cellular and cytokine environment (*25*). The effects of the
189 TdLN on TCR–pMHC 2D affinity on donor $CD45.2^+$ $CD8^+$ OT-I T cells recovered 7 days post
190 adoptive transfer into $CD45.1^+$ recipient animals co-implanted with (Tumor, Fig. 2E, left) or
191 without (Naïve, Fig. 2e, right) B16F10 tumors were evaluated by the micropipette adhesion
192 frequency (MAF) assay (*17, 39*). MAF employs a human red blood cell (RBC) coated with pMHC
193 as a surrogate tumor cell to interact with the T cell, which were respectively aspirated by two
194 opposing micropipettes (Fig. 2F). The ultrasoft RBC acts as a force transducer to detect TCR–
195 pMHC binding from RBC elongation after its retraction from contact with the T cell. Instead of
196 H2-$K^b$, a mutant H2-$K^b$α3A2 was used to present the OVA peptide SIINFEKL, which replaced
197 the mouse α3 domain of H2-$K^b$ by that of human HLA-A2, in order to abolish any mouse CD8–
198 MHC interaction (*17*). Each T cell was repeatedly contacted by the RBC 50 times to determine an
199 adhesion frequency from which a 2D affinity was evaluated (*17, 39*). Similar TCR–pMHC 2D
200 affinities were found from donor $CD8^+$ OT-I T cells isolated from LNs and spleens of naïve
201 recipient animals; however, significantly lower 2D affinities were found from OT-I $CD8^+$ T cells
202 isolated from TdLNs than spleens of the same tumor-bearing recipient animals (Fig. 2G). This
203 shows that the TdLN diminished TCR binding affinity for antigen pMHC, explaining, at least in

204 part, the observed TME suppression of $CD8^+$ T cell activation in vivo (Fig. 1E, F, H-M) and in
205 vitro (Fig. 2B, C).

206 **Characterization of TME suppression of TCR–pMHC and TCR–pMHC–CD8 interactions**

207 To further characterize the localized suppressive effects of tumor and TdLN on TCR antigen
208 recognition, TCR 2D affinity for antigen pMHC was systematically evaluated comparing among
209 $CD8^+$ T cells recovered from tumors, TdLNs, non-tumor associated LNs (NdLNs), the spleen and
210 blood. For these experiments, B16F10 cells not expressing the OVA antigen were directly
211 implanted into OT-I mice and the endogenous $CD8^+$ T cells were isolated from compartments of
212 interest at various days post tumor implantation for MAF analysis (Fig. 3A). This model was used
213 to overcome the overall low levels of donor cell recovery in the adoptive transfer models (Fig. 1G,
214 2E), yielding as many as 100-fold $CD8^+$ T cells expressing OT-I TCR specific for SIINFEKL:H2-
215 $K^b$ from not only lymphoid tissues but also the tumor itself. B16F10 melanoma growth in the two
216 tumor-recipient mouse strains was comparable (Fig. S1A). Lymphoid tissues including TdLNs
217 (Fig. S1B) and spleen also exhibited no gross differences in the frequencies of major immune cell
218 types except for decreased macrophage and increased B lymphocyte frequencies in OT-I animals
219 relative to C57BL/6 animals (Fig. S1C). Immune phenotyping the melanoma-implanted OT-I and
220 C57BL/6 mice over the course of tumor development also revealed no significant differences in
221 the numbers of $CD8^+$ T cells infiltrating the tumor, within TdLN or spleen between the OT-I and
222 C57BL/6 mice, except for a mild expansion of $CD8^+$ T cells in the spleen of OT-I animals from
223 d7 to d11 post tumor implantation (Fig. S1D). No gross differences were found in antigen
224 activation phenotypes as assessed by the numbers of PD-1 (Fig. S1E) or CD25 (Fig. S1F)
225 expressing $CD8^+$ T cells, except for an increase in splenic PD-$1^+CD8^+$ population in OT-I animals

226 at d11. However, the number of $CD4^+$ T cells were ~10-fold lower in OT-I than C57BL/6 animals
227 (Fig. S1G), including $CD25^+Foxp3^+CD4^+$ regulatory T cells (Tregs) (Fig. S1H), as expected (*40*).
228 The number of myeloid-derived suppressor cells (MDSCs) and PD-1 ligand-1 (PD-L1)-expressing
229 lymphocytes ($PD\text{-}L1^+CD45^+$) were equivalent between analyzed tissues of OT-I and C57BL/6
230 animals throughout tumor progression, except for subtle increases in in spleens or tumors of the
231 OT-I animals on d7-d11 or d11 respectively (Fig. S1I-J). Thus, the abundance and phenotype of
232 $CD8^+$ T cells as well as immune suppressive cell subsets are roughly similar for OT-I and C57BL/6
233 tumor-bearing mice, indicating similar TMEs established in both C57BL/6 and OT-I hosts.

234 The TCR–SIINFEKL:H2-$K^b$α3A2 2D affinities were measured by the MAF assay (Fig.
235 2F) using $CD8^+$ T cells isolated from various tissue compartments of OT-I mice. Cells from tumor
236 and TdLNs had much lower affinities than those from NdLN, spleen, and blood (Fig. 3B), agreeing
237 with previous results (Fig. 2G) obtained using the model in which OT-I donor cells were adoptively
238 transferred into melanoma-bearing C57BL/6 recipients and harvested from the TdLN 7 days post
239 tumor implantation (Fig. 2E). Furthermore, $CD8^+$ T cells from NdLN, spleen, and blood of tumor-
240 bearing OT-I mice exhibited comparable TCR–pMHC 2D affinities to that of $CD8^+$ T cells isolated
241 from LNs of tumor-free OT-I mice (Fig. 3B), suggesting the local nature of this suppressive effect
242 that is limited to the tumor and TdLN. However, MHC–CD8 2D affinities measured using a null
243 pMHC (VSV:H2-$K^b$) not recognized by the OT-I TCR showed no compartmental differences (Fig.
244 3C), isolating the TME-induced defect to the TCR molecule. Moreover, OT-I T cells from TdLN
245 and NdLN generated similar levels of binding frequencies to an anti-TCR Vα2 antibody (Fig. 3D),
246 indicating the antigen-specific nature of this suppressive effect that impairs the ability for the TCR
247 to recognize antigen. Still, when OT-I T cells were tested against SIINFEKL:H2-$K^b$ to allow CD8
248 to interact with the MHC to form TCR–pMHC–CD8 trimolecular bonds (*18, 41*), a decrease in the

249 average number of bonds (<*n*>) normalized by the densities of TCR ($m_{TCR}$) and pMHC ($m_{pMHC}$)
250 was again observed using $CD8^+$ T cells from NdLN to TdLN (Fig. 3E). However, the
251 compartmental differences between NdLN and TdLN disappeared when the 2D affinities of CD8
252 to bind MHC pre-bound by TCR were compared (*42*) (Fig. 3F). Thus, the impaired TCR–pMHC–
253 CD8 trimolecular interaction can be attributed to a reduced TCR–pMHC 2D affinity rather than
254 the synergy between TCR and CD8 for pMHC binding. Finally, the reduced TCR–pMHC 2D
255 affinity of $CD8^+$ T cells from NdLNs to TdLNs was detectable as early as d3 post tumor
256 implantation, and was sustained in OT-1 mice bearing d11 tumors (Fig. 3G). This reduction in
257 TCR–pMHC 2D affinity ranged from 20-40% in d3, d7, and d11 post tumor implantation (Supp
258 Fig. 2A). Thus, antigen recognition by $CD8^+$ T cells was persistently suppressed during tumor
259 progression in both tumor and TdLN as signified by the decreased TCR–pMHC bimolecular
260 affinity and TCR–pMHC–CD8 trimolecular avidity. Note that 2D affinity differences were found
261 despite no difference in TCR expression and staining by tetramers with SIINFEKL:H-$2K^b$ and
262 SIINFEKL:H-$2K^b$α3A2 on T cells isolated from various tissues of tumor-bearing and -naive OT-
263 I mice (Fig. S2B-C), consistent with previous findings that 2D analysis is superior to tetramer
264 analysis (*18, 21, 25*).

265 Transforming growth factor (TGF) β in TME is known to play pleiotropic roles, including
266 modulating tumor growth and the functions of $CD8^+$ T cells (*43-45*). TGF-β has furthermore been
267 shown to be a determinant of the differential TCR–pMHC 2D affinities of $CD8^+$ T cells from
268 splenic red pulp and white pulp of virial infected mice (*25*) and to negatively regulate tumor-
269 specific $CD8^+$ T cell cytotoxicity (*46*). The effect of inhibiting TGF-β signaling on TCR–pMHC
270 2D affinity was examined through daily intraperitoneal injection of TGF-β R1 inhibitor SB431542
271 in OT-I mice bearing B16F10 melanomas (Fig. 4A). In contrast to vehicle controls, the difference

272 in TCR–pMHC 2D affinities between $CD8^+$ T cells from TdLNs and NdLNs of TGF-β R1 inhibitor
273 treated animals was no longer observed (Fig. 4B). This implicates the TME-related soluble factor
274 TGF-β in deficient $CD8^+$ T cells antigen recognition.

275 **TdLN suppresses $CD8^+$ T cells pulling forces on antigen pMHC**

276 To elicit anti-tumor immunity, T cells must interact physically with tumor cells. Upon engaging
277 their TCR with (neo)antigenic pMHC, T cells may exert endogenous forces on the TCR–pMHC
278 and TCR–pMHC–CD8 bonds as part of their mechano-sensing and -responsive processes, which
279 has been observed *in vitro* using DNA-based molecular tension probes (MTP) (*47, 48*). MTPs are
280 a class of powerful tools for measuring ligand-induced, signaling-dependent, and actomyosin-
281 powered endogenous forces exerted by the cell on the receptor–ligand bonds (*49-51*). An MTP
282 consists of a fluorophore-quencher pair flanking a DNA hairpin to unfold at a designed tension
283 adjustable by changing the GC contents and length of the DNA strands (*49, 52, 53*) (Fig. 5A). One
284 end presents a ligand or antibody to the cell surface receptor and the other end is linked to the
285 cover glass *via* a gold nanoparticle to further quench the fluorophore (e.g., Cy3B). Forced-
286 unfolding of the DNA-hairpin de-quenches the Cy3B to yield a fluorescent signal, thereby
287 reporting an above-threshold tension exerted on the receptor by the cell (Fig. 5A). The fluorescent
288 intensity is proportional to the number of unfolded DNA hairpins, hence reads out the ability of
289 the TCR and/or CD8 to bind, stay engaged, and be activated by pMHC, and of the T cell to generate
290 and apply above threshold forces on the TCR–pMHC and TCR–pMHC–CD8 bonds, all of which
291 are features of $CD8^+$ T cells that we would like to test whether TME would suppress.

292 $CD8^+$ T cells from TdLNs or NdLNs of OT-I mice bearing d7 B16F10 tumors (Fig. 3A)
293 were placed on glass surface functionalized with SIINFEKL:H2-$K^b$ tagged by MTP of a 4.7 pN

294 threshold force. Twenty min post cell seeding, the area of T cell spreading was measured by
295 reflection interference contrast microscopy (RICM) and the average fluorescence intensity over
296 that area was measured by total internal reflection fluorescence (TIRF) microscopy (Fig. 5B). As
297 shown by the quantification obtained from a large number of cells, $CD8^+$ T cells from TdLNs were
298 found to spread less (Fig. 5C) and pull on less pMHC molecules with >4.7 pN forces (Fig. 5D)
299 than cells from NdLNs. Remarkably, no such differential spreading areas and force signals
300 between TdLN and NdLN $CD8^+$ T cells were observed when the MTP tag was changed from the
301 SIINFEKL:H2-$K^b$ ligand to an anti-TCR antibody (Fig. 5C, D). The antigen-specific nature of
302 these two differential readouts correlates with that of the differential TCR interactions with pMHC
303 and lack of difference of TCR interactions with the same anti-TCR antibody (Fig. 3B, D),
304 supporting a hypothetical relationship between the TdLN impaired TCR 2D affinity and the TdLN
305 impaired T cell activation, spreading as well as force generation, transmission, and exertion on
306 pMHC.

307 **TdLN suppresses calcium signaling of $CD8^+$ T cells stimulated by antigen pMHC**

308 To directly test the hypothesis that TdLN impairs antigen-induced T cell activation, OVA pMHC-
309 triggered calcium signaling of $CD8^+$ T cells from TdLNs and NdLNs of OT-I mice bearing d7
310 B16F10 melanomas (Fig. 3A) were compared. T cells were loaded with a calcium indicator Fluo-
311 4 and a microfluidic cell trap array device was used to place them on polydimethylsiloxane (PDMS)
312 surfaces functionalized with SIINFEKL:H2-$K^b$ or bovine serum albumin (BSA) as control (Fig.
313 6A, *top*) (*54*). Calcium signals of cells imaged in the field of view were recorded continuously for
314 10 min in real-time at the single-cell level by their fluorescence intensity (Fig. 6A, *bottom*). For
315 each cell, the moment when a cell settled into the cell trap was defined as "t = 0". The fluorescence

316 intensity time-courses for different cells were realigned to their respective starting times, which
317 were displayed on a heatmap as columns and sorted in ascending cumulative calcium intensity
318 across rows, clearing showing that T cells generated calcium responses to pMHC but not BSA
319 (Fig. 6B).

320 Despite cell-to-cell variation, the overall calcium response to SIINFEKL:H2-$K^b$ was much
321 weaker for $CD8^+$ T cells from TdLNs than NdLNs of the same tumor-bearing animal (Fig. 6B,
322 right panels). This can also be seen in the averaged calcium fluorescent intensity (FI) vs time (Fig.
323 6C) and the FI accumulation over time for all individual cells (Fig. 6D), both of which were much
324 lower for $CD8^+$ T cells from TdLNs than NdLNs. As a positive control, $CD8^+$ T cells from both
325 tissue sources on BSA surfaces were stimulated by ionomycin, which showed robust and rapid
326 calcium signals (Fig. 6E), displaying high levels of calcium signals without compartmental
327 difference (Fig. 6F-G). Thus, rather than a TdLN-induced defect in the T cell's intrinsic ability to
328 flux calcium, the diminished calcium responses of $CD8^+$ T cells from TdLNs is specific to defects
329 in their capacity to recognize and respond to antigen. Together, these data indicate the reduced
330 downstream signaling following TCR triggering in $CD8^+$ T cells freshly isolated from the TdLN
331 relative to NdLN.

332 **TdLN suppresses TCR 2D affinity and function of antigen-experienced $CD8^+$ T cells**

333 In the preceding sections, an "antigen-inexperienced" model where $CD8^+$ T cells isolated from
334 OT-I mice bearing B16F10 melanoma without the prior encountering of its cognate antigen *in vivo*
335 was used to examine the TME effects *in vitro* for binding to (Figs. 3 and 4), pulling on (Fig. 5),
336 and fluxing calcium on (Fig. 6) OVA pMHC. Whether the TME exerted similar effects on
337 "antigen-experienced" $CD8^+$ T cells was also explored using three models of *in situ* antigen

338 recognition (Fig. 7A, D and G). In the first model, $CD8^+$ T cells from $CD45.2^+$ OT-I donor mice
339 were adoptively transferred into $CD45.1^+$ C57BL/6 recipient animals co-implanted in the lateral
340 dorsal skin with B16F10 cells (Tumor) or left untreated (Naïve). Three days later, animals were
341 immunized with Ag-NPs and Toll-like receptor ligand CpG-NP into the forelimb skin, a regimen
342 we have previously shown to elicit robust $CD8^+$ T cell immunity functional in mediating control
343 of B16F10 melanomas (*37*). After 7 days post adoptive transfer (4 days post immunization), donor
344 cells were harvested from the spleens and LNs and analyzed by FACS for activation markers and
345 MAF for 2D affinity (Fig. 7A). The immunization step caused a population of $CD8^+$ T cells to
346 experience Ag stimulation *in vivo*. Whereas only small percentage of endogenous $CD8^+$ T cells of
347 the tumor-naïve $CD45.1^+$ recipient mice isolated from the spleen and LN were CD44 positive, an
348 indicator of activation by antigen (Fig. 7B, green), nearly all donor cells ($CD45.2^+$) from both the
349 spleen and LN of the recipient animals were CD44 positive (Fig. 7B, red). MAF experiments found
350 lower OT-I TCR–SIINFEKL:H2-$K^b$α3A2 2D affinity of donor cells from TdLNs than spleens of
351 d7 B16F10 melanoma bearing animals; however, no such difference was found in tumor-naive
352 recipient animals (Fig. 7C). This data indicates that TME locally suppresses TCR 2D affinity of
353 $CD8^+$ T cells primed by antigen *in vivo*.

354 The functional responses of $CD8^+$ T cells that had previously experienced antigen to
355 antigen re-exposure was assessed by the second model (Fig. 7D). Cell suspensions harvested from
356 various tissues of tumor-bearing or -naïve $CD45.1^+$ C57BL/6 recipient animals that had received
357 adoptive transfer of $CD8^+$ T cells from $CD45.2^+$ OT-I mice and subsequently injected with
358 SIINFEKL-NPs into the d7 B16F10 melanoma or naïve skin, respectively, were restimulated *ex*
359 *vivo* using SIINFEKL peptide. In response to antigen restimulation, fewer donor cells from TdLNs
360 of tumor-bearing mice than LNs of tumor-naïve mice produced TNF-α, IL-2, and GzmB, although

361 similar numbers of cells produced INF-γ were found in the same two sites (Fig. 7E), implying
362 decreased functional responsiveness by T cells in the tumor-draining vs naïve LN
363 microenvironment. By comparison, donor cells recovered from spleens of tumor-bearing vs -naive
364 animals exhibited no differences in TNF-α, IFN-ɣ, IL-2, and GzmB producing cells (Fig. 7F). This
365 indicates that TME locally suppresses functional responses of antigen-experienced $CD8^+$ T cells
366 to antigen restimulation.

367 TCR 2D affinities were compared by the MAF experiments using the third model (Fig.
368 7G). $CD8^+$ T cells from $CD45.2^+$ OT-I mice were adoptively transferred into $CD45.1^+$ C57BL/6
369 mice one day prior to implantation with B16F10-OVA melanoma cells. Donor cells isolated from
370 TdLNs of recipients bearing d7 B16F10-OVA tumors exhibited a reduced TCR–pMHC 2D
371 affinity compared to those from the spleen (Fig. 7H), consistent with previous results when the
372 B16F10 melanoma implanted in the recipients was not conjugated with OVA antigen and hence
373 the recovered donor cells were antigen-inexperienced. However, donor T cells harvested from
374 NdLNs also displayed a lower TCR–pMHC 2D affinity than those harvested from spleens of the
375 same recipient (Fig. 7H), in contrast to antigen-naïve models. Collectively, the results showed that
376 the TME impairment of antigen recognition impacts $CD8^+$ T cells not only at naïve stages but also
377 after *in vivo* antigen activation.
378

379 **Discussion**

380 Despite a functional systemic immunity, the melanoma TME is known to suppress its effects to
381 allow disease progression (*55*). In the workhorse model of the melanoma immunotherapy field
382 implemented in this work, antigen-induced activation and anti-tumor responses of $CD8^+$ T cells *in*
383 *vivo* was likewise suppressed by the TME. Whereas many cell intrinsic and extrinsic factors
384 contribute the said suppression (*4, 5, 56*), our data reveal a new defect caused by the TME – the
385 impaired T cell antigen recognition, manifested a reduced TCR–pMHC 2D affinity and bonds
386 pulled by >4.7 pN T cell-generated forces measured *ex vivo.* This was further correlated
387 functionally with a lower intracellular calcium signaling induced by *in vitro* antigen stimulation.
388 These findings collectively indicate the impaired antigen recognition as a novel mechanism of T
389 cell dysfunction in the TME. Interestingly, this newly identified effect of TME suppression of
390 TCR antigen recognition may explain two puzzling observations of a recent study of adoptive cell
391 therapy (ACT) of tumor patients (*57*). The authors reported that $CD8^+$ T cells that were transfected
392 with the same TCRs specific to tumor neoantigen, expanded in vitro, and used in ACT to treat
393 cancer patients were more effective if 1) the original T cells were isolated from healthy individuals
394 than from the patients themselves and 2) the original T cells were isolated from peripheral blood
395 lymphocytes than from TILs of the same patient (*57*). The explanation based on the present work
396 could be that the latter T cells had been subjected to the TME suppression whereas the former T
397 cells had not in both cases.

398 The finding that $CD8^+$ T cells from d3-d11 tumors and TdLNs (collectively referred to as
399 TME) exhibit reduced *in situ* affinity of TCR for specific pMHC is particularly intriguing. Previous
400 studies have shown correlation of 2D TCR–pMHC affinity with T cell activation and functions

401 using altered peptide ligands (*17-23*). Unlike 3D affinity measured using soluble proteins, 2D
402 TCR–pMHC affinity can be altered by perturbations of the T cell cellular environment (*17, 24,*
403 *25*). Of particular relevance to the present work, the P14 TCR–gp33:H2-$D^b$ 2D affinity of
404 adoptively transferred $CD8^+$ T cells was found to be higher when donor cells were isolated from
405 splenic red pulp than white pulp of C57BL/6 recipients post lymphocytic choriomeningitis virus
406 infection. The increased antigen recognition of red pulp-derived $CD8^+$ T cells correlates with a
407 more efficient target cell killing *in vitro* and improved viremia control *in vivo*, whereas the
408 decreased antigen recognition of white pulp-derived $CD8^+$ T cells anti-correlates with their
409 enhanced ability to differentiate to memory cells (*25*). Like the previous studies (*25*), differences
410 in 2D affinity were not detectable by saturating pMHC tetramer staining, supporting the contention
411 that 2D measurements made herein provide greater power to distinguish functionally relevant
412 differences in binding propensities of TCR–pMHC interactions.

413 The TCR–pMHC–CD8 trimolecular avidity was also reduced by the TME, yet the CD8
414 affinities for both free MHC and TCR-bound MHC were not, isolating the TME-caused defects to
415 the TCR itself. T cells can be activated by anti-TCR antibodies, yet the 2D binding of an anti-TCR
416 antibody to TCR was not impacted, highlighting the specificity of the TME suppression on the
417 ability of TCR to recognize antigen instead of being recognized as an antigen.

418 T cells spontaneously sample and exert forces on pMHC-coated surfaces. Such forces are
419 transmitted through the TCR–pMHC complexes and thought to play a key role in antigen
420 discrimination (*47, 48*). T cell spreading and pulling on pMHC was reduced by the TME, likely
421 caused in part by the TME-suppressed TCR–pMHC and TCR–pMHC–CD8 interactions, because
422 neither T cell spreading/pulling on anti-TCR antibody nor TCR–anti-TCR antibody interaction

423 was suppressed by the TME. Reduced T cell spreading and pulling may be caused by the TME
424 impairment of not only the recognition of, but also the response to, antigen by the T cell, which
425 includes T cell signaling. This contention is supported by the results that only the calcium signaling
426 of T cells stimulated by pMHC but not by ionomycin was reduced by the TME. Thus, the MTP
427 experiments provide two additional readouts for the TME impairment of TCR recognition of, and
428 activation by, antigen pMHC.

429 Chronic tumor antigen stimulation leading to T cell exhaustion is a well-known contributor
430 to T cell dysfunction in the TME (*58*). However, we found that TME impaired antigen recognition
431 by not only antigen-experienced but also antigen-inexperienced $CD8^+$ T cells. In the absence of
432 OVA-expression by tumor cells, antigen-naïve donor OT-I $CD8^+$ T cells suppressed by B16F10
433 melanomas in recipient mice were not exhausted as evidenced by the low expression of PD-1.
434 After isolation from the TME, these antigen-naïve cells encountered antigen the first time during
435 the measurements for TCR–pMHC 2D affinity, endogenous force pulling on the TCR or calcium
436 response, or during the *ex vivo* stimulation for functional assays. Since any donor T cells from any
437 TCR transgenic mice can first be adoptively transferred to antigen-free tumor-bearing recipient
438 mice and later be probed by the pMHC specific for this TCR to observe the TME effects, such
439 suppressive effects must exert on all T cells of any antigen specificity. Thus, tumors can suppress
440 the antigen recognition and function of T cells that do not recognize and react against the tumor
441 itself, and this mechanism is independent of the T cell exhaustion due to chronic tumor antigen
442 stimulation. This implies that the TME suppresses local $CD8^+$ T cell immunity in general, not just
443 that against tumor.

444 As a first step toward elucidating the mechanism underlying the TME suppression of T cell
445 recognition of and response to antigen, we tested the role of TGF-β, a TME-associated
446 immunosuppressive factor. The localized impairment of T cell antigen recognition was partially
447 restored by inhibiting the TGF-β signaling. This indicates that, in addition to its other known
448 effects in TME (*4, 5, 56*), TGF-β also negatively regulates all $CD8^+$ T cells' TCR–pMHC 2D
449 affinities regardless of the TCR specificity. This agrees with our previous results that *in vivo*
450 inhibition of TGF-β activity eliminates the differences in the TCR–pMHC 2D affinities between
451 $CD8^+$ T cells from splenic red and white pulps of virus infected $CD8^+$ T cells and that *in vitro*
452 treatment with recombinant TGF-β reduces TCR–pMHC 2D affinity (*25*). As the tumor progresses,
453 TGF-β in the TME accumulates in the TdLN, which can affect any peripheral T cells trafficking
454 through the TdLN. Comparing to other identified suppressive factors causing T cell tolerance,
455 TGF-β is antigen-independent, unlike chronic tumor-antigen stimulation; and it does not require
456 direct cell-cell contact between an immunosuppressive cell and the T cell, unlike nitration of
457 tyrosine in TCR by MDSCs (*59*).

458 Together, our data uncover impaired T cell recognition of and response to antigen as a
459 novel mechanism of T cell dysfunction in the TME. This mechanism is independent of T cell
460 exhaustion induced by chronic tumor antigen stimulation and affects both antigen-inexperienced
461 and antigen-experienced T cells irrespective of their antigen specificity. More importantly, the
462 impaired T cell antigen recognition is a cause and an indicator of TME induced T cell dysfunction,
463 which can be regulated by remodeling the soluble factor TGF-β in the TME. Our findings thus
464 have implications for future studies seeking to identify TME extrinsic factors that suppress T cell
465 function through altered TCR–pMHC 2D affinity and responses. Our results also implicate that

466 the alteration of antigen recognition by $CD8^+$ T cells can potentially serve as an additional metric

467 for characterizing the TME and its amenability to immunotherapy.

468

469

470 **Methods**

471 **Cell culture**

472 B16F10 or B16F10-OVA mouse melanoma cells were maintained in culture in Dulbecco's
473 Modified Eagle Medium (DMEM, Gibco, Thermo Fisher Scientific, Inc., Waltham, MA) with 10%
474 heat-inactivated fetal bovine serum (FBS, Gibco, Thermo Fisher Scientific, Inc.) and 1%
475 penicillin/streptomycin/amphotericin B (Life Technologies, Carlsbad, CA, USA). Cells were
476 passaged at ~80% confluency and maintained at 37 ºC with 5% $CO_2$ in a standard cell incubator.

477 **Animal tumor models**

478 CD45.2$^+$ OT-I transgenic mice were obtained from Charles River Laboratory (Lyon, France) and
479 bred in house at the Georgia Institute of Technology. C57BL/6 and CD45.1$^+$ C57BL/6 mice were
480 purchased at 6 weeks (wk) of age from the Jackson Laboratory (Bar Harbor, ME, USA). All
481 protocols were approved by Georgia Tech's Institutional Animal Care and Use Committee
482 (IACUC) and have been previously described (*26, 38*). For tumor-bearing cohorts, $0.5 \times 10^6$
483 melanoma cells were intradermally injected into the left dorsal skin of 6-8 wk old mice. Tumor
484 dimensions were measured with calipers in three dimensions and reported as ellipsoid volume.

485 **Flow cytometry**

486 Axillary and brachial LNs were pooled and incubated with 1 mg/mL Collagenase D (Sigma-
487 Aldrich) in Dulbecco's phosphate buffered saline (D-PBS) with calcium and magnesium for 75
488 min at 37 ºC, passed through a 70 µm cell strainer (Greiner Bio-One, Monroe, NC, USA), washed,
489 and resuspended in a 96-well U-bottom plate (VWR International, Inc.) for staining. Spleen

490 capsules were disrupted using 18G needles (Beckton Dickinson, Franklin Lakes, NJ), and pushed
491 through a 70 µm cell strainer, then pelleted and resuspended in RBC lysis buffer (Sigma-Aldrich)
492 for 7 min at room temperature, diluted with D-PBS, washed, and 5% of the spleen plated in a 96-
493 well U-bottom plate. Tumor samples were incubated with 1 mg/mL Collagenase D (Sigma-Aldrich)
494 in D-PBS for 4 h at 37 ºC, passed through a 70 µm cell strainer, washed, and 1-20% (based on
495 tumor volume) plated in a 96-well U-bottom plate for staining. All antibodies for flow cytometry
496 were obtained from Biolegend, Inc. (San Diego, CA, USA). Cells were blocked with anti-mouse
497 CD16/CD32 (clone: 2.4G2) (Tonbo Biosciences, San Diego, CA, USA) for 5 min on ice and
498 washed. Samples were then stained using fixable viability dye Zombie Aqua (1:100, Biolegend)
499 for 30 min at room temperature before quenching with 0.1% bovine serum albumin (BSA) in D-
500 PBS (flow cytometry buffer). Antibodies were prepared in flow cytometry buffer at the following
501 dilutions based on preliminary titrations: PerCP anti-mouse CD3 (1:40), APC-Cy7 anti-mouse
502 CD4 (1:640), FITC anti-mouse CD8 (1:320), PE-Cy7 anti-mouse CD25 (1:100), and APC anti-
503 mouse PD-1 (1:80) to assess T cells in Fig. S1; APC-Cy7 anti-mouse CD45 (1:160), PerCP anti-
504 mouse F4/80 (1:20), PE anti-mouse CD169 (1:50), APC anti-mouse Gr1 (1:80), PE-Cy7 anti-
505 mouse CD11c (1:80), BV421 anti-mouse PD-L1 (1:40), FITC anti-mouse B220 (1:400), and
506 AF700 anti-mouse CD11b (1:80) to assess pan immune cells in Fig. S1; PerCP anti-mouse CD69
507 (1:80), BV711 anti-mouse CD45.2 (1:80), BV605 anti-mouse CD3 (1:100), APC-Cy7 anti-mouse
508 CD8 (1:40), and BV786 anti-mouse PD-1 (1:80) for intracellular cytokine staining in Figs. 2B-D
509 and 7E-F; and PE anti-mouse CD45.2 (1:80), AF700 anti-mouse CD25 (1:100), BV785 anti-mouse
510 PD1 (1:80), AF647 anti-mouse CXCR5 (1:200), PerCP anti-mouse CD3 (1:40), APC-Cy7 anti-
511 mouse CD8 (1:40), PE-Cy7 anti-mouse CD39 (1:20), and BV421 anti-mouse CD44 (1:20) for T
512 cell phenotyping in Fig. 1. Cells were fixed in 2% paraformaldehyde (VWR International, Inc.) to

513 assess pan-immune cells in Fig. S1. For nuclear staining, cells were incubated with
514 FoxP3/Transcription Factor Fixation/Permeabilization solution (eBioscience, ThermoFisher, Inc.)
515 for 60 min on ice in dark. Cells were then incubated with PE anti-mouse FoxP3 (1:20) for T cell
516 phenotyping in Fig. 1 and Fig. S1 in FoxP3/Transcription Factor Fixation/Permeabilization buffer
517 for 75 min on ice in dark. For *ex vivo* cytokine staining, cells were suspended in IC Fixation Buffer
518 (eBioscience, Thermo Fisher, Inc.) for 60 min at room temperature in dark. Cells were then
519 incubated with APC anti-mouse GzmB (1:40), PE anti-mouse IFN-γ (1:80), AF700 anti-mouse
520 IL-2 (1:200), and PE-Cy7 anti-mouse TNF-α (1:80) in IC Permeabilization Buffer (eBioscience,
521 Thermo Fisher, Inc.) for 60 min at room temperature in dark. Cells were then resuspended in FACS
522 buffer (1% BSA in D-PBS) and kept at 4ºC in dark until analyzed with a customized BD LSR
523 Fortessa flow cytometer (BD Biosciences). Compensation was performed using ArC and
524 UltraComp compensation beads (Thermo Fisher Scientific, Inc.) and data was analyzed using
525 FlowJo software v9 and v10 (FlowJo, LLC, Ashland, OR, USA).

526 **$CD8^+$ T Cell Isolation**

527 OT-I animals were sacrificed by $CO_2$ asphyxiation. For adoptive transfer, spleens were dissected
528 and placed into sterile PBS. Spleens were digested using 18G needles (Beckon Dickinson), and
529 pushed through 70 μm cell strainers, washing liberally with PBS. RBCs were lysed using AcK
530 Lysis Buffer (Lonzo Group AG, Basel, Swirzerland), and washed with PBS. After counting, cells
531 were resuspended in FACS buffer (1% BSA in PBS) at a concentration of $10^8$ cells/mL and 1 μL
532 negative $CD8^+$ T cell biotin-antibody cocktail (Biolegend)/million cells was added and allowed to
533 incubate for 15 min on ice. Streptavidin-magnetic beads were added directly to this solution at a
534 concentration of 1 μL/million cells and allowed to incubate for 15 min on ice. PBS +/+ was then

535 added for a final volume of 2.5mL and the mixture placed in magnetic separators. The flow-
536 through was then collected, counted, and resuspended. CFSE was added to the cells for 6 minutes,
537 followed by quenching with ice cold RPMI medium containing >10% heat-inactivated FBS (Life
538 Technologies). Purity, viability, and CFSE loading (if applicable) were confirmed using a
539 customized BD LSR Fortessa flow cytometer prior to transfer. Cells were maintained in sterile
540 conditions prior to transfer.

541 For the $CD8^+$ T cell isolation in MAF, MTP, and microfluidic calcium assays, organs of
542 OT-I mice were mechanically digested into cell suspension, and $CD8^+$ T cells were negative
543 purified from cell suspension with untouched $CD8^+$ T cell isolation kit (Stemcell Technologies).
544 For the isolation of donor $CD45.2^+$ OT-I T cells from C57BL/6 $CD45.1^+$ recipient animals, the
545 selection was achieved by antibody labeled sorting based on congenic marker.

546 **Adoptive Transfer**

547 Isolated $CD8^+$ T cells were suspended in sterile saline at a concentration of $2 \times 10^6$ cells/200μL.
548 After isoflurane anesthesia, the hair covering the jugular vein of animals was removed using
549 depilatory cream, cleaned using warm water and ethanol wipes, and suspended cells injected
550 intravenously via the jugular vein.

551 **TGF-β signaling inhibition**

552 The animals were injected with TGF-β RI Kinase Inhibitor SB431542 (Sigma-Aldrich) at 10
553 mg/kg in 100 μl DMSO intraperitoneally for continuous three days.

554 **Micropipette adhesion frequency assay**

555 The micropipette adhesion frequency (MAF) assay for measuring receptor–ligand 2D affinity has
556 been described (*17, 39*). Briefly, human RBCs were biotinylated with controled concentration of
557 biotin-X-NHS linker (Millipore/Sigma). The biotinylated RBCs were sequentially incubated with
558 saturating amount of streptavidin (ThermoFisher) and the biotinylated proteins of interest. An RBC
559 coated with ligand (L) and a T cell expressing receptor (R) were respectively aspirated by two
560 apposing glass micropipettes (Fig. 2F). The two cells were brought into 50 contact-and-retract
561 cycles by one of the micropipettes mounted to a piezoelectric translater controlled by a computer.
562 The adhestion frequency ($P_a$) was calculated by number of adhesion events appeared in the total
563 of 50 contacts, where the adhesion events were detected by the deflection of the soft RBC
564 membrane during micropiette retraction. The averaged number of bonds formed per contact $\langle n \rangle$
565 is calculated as:

566 $$\langle n \rangle = -\ln(1 - P_a) \qquad \text{Eq. 1}$$

567 In the case of bimolecular interaction, the interaction kinetics is described by a probabilistic
568 kinetics model:

569 $$\langle n \rangle = m_R m_L A_c K_a [1 - \exp(-(k_{off} t_c)] \qquad \text{Eq. 2}$$

570 where $A_c$ (in μm$^2$) and $t_c$ (in s) are contact area and time, respectively, controlled by the
571 experimenter, $K_a$ (in μm$^2$) and $k_{off}$ (in s$^{-1}$) are 2D affinity and off-rate, respectively, $m_R$ and $m_L$ (in
572 μm$^{-2}$) are molecule densities of the receptor and ligand, respectively, determined from comparing
573 the mean fluorescence intensity (MFI) of saturating amount of antibody staining of targeted
574 proteins, to those of calibration beads (BD Biosciences). $P_a$ reaches steady-state at $t_c \gg 1/k_{off}$ when
575 $\exp(-k_{off} t_c) \rightarrow 0$, $\langle n \rangle \rightarrow m_R m_L A_c K_a$. Based on previous study (*17*), $P_a$ reached plateau when $t_c > 1$

576 s for the OT-I TCR–SIINFEKL:H2-K$^b$α3A2 interaction. Therefore, we report the values of
577 effective 2D affinity $A_cK_a$ (in μm$^4$) calculated from the equation below using $P_a$ measured at 2 s.

578 $$A_cK_a = -\ln(1 - P_a)/m_R m_L \quad \text{Eq. 3}$$

579 In the case where CD8$^+$ OT-I T cells was allowed to interact with RBCs bearing
580 SIINFEKL:H2-K$^b$, <*n*> includes three species of bonds, TCR–pMHC and CD8–MHC bimolecular
581 bonds and TCR–pMHC–CD8 trimolecular bonds (*18, 41, 48*). Neglecting the CD8–MHC bond
582 species because of its orders of magnitude lower affinity than those of the other two bond species,
583 we can express the average number of total bonds at steady-state by (*42*):

584 $$\langle n \rangle = m_{\mathrm{TCR}} m_{\mathrm{pMHC}} A_c K_{\mathrm{a,TCR}} \left(1 + m_{\mathrm{CD8}} A_c K^*_{\mathrm{a,CD8}}\right) \quad \text{Eq. 4}$$

585 where $K^*_{\mathrm{a,CD8}}$ is the 2D affinity for CD8 to bind MHC pre-bound by TCR and $m_{\mathrm{CD8}}$ is the site
586 density of CD8. $K^*_{\mathrm{a,CD8}}$ can solved from Eq. 4:

587 $$K^*_{\mathrm{a,CD8}} = \left(\frac{\langle n \rangle}{m_{\mathrm{TCR}} m_{\mathrm{pMHC}} A_c K_{\mathrm{a,TCR}}} - 1\right) / m_{\mathrm{CD8}} \quad \text{Eq. 5}$$

588 **DNA-based molecular-tension probe**

589 The DNA-based molecular tension probes (MTP) were assembled as previously described (*47, 48,*
590 *60*). Briefly, three strands of oligonucleotides, the 4.7 pN hairpin strand, the Cy3B strand with
591 biotin on the opposite end of the Cy3B dye, and the Black Hole Quencher-2 (BHQ2) strand, were
592 mixed and annealed at a ratio of 1.1:1:1.1, with additional BHQ2 strand added after the annealing
593 to further lower the background. The DNA-based MTP was then immobilized onto gold
594 nanoparticles irreversibly anchored on APTES-PEG modified glass surface (*47*). The surface was

595 sequentially incubated with streptavidin and biotinylated pMHC ligands or antibodies to tag them
596 to the MTPs through biotin-streptavidin coupling. Working solution, incubation time and washing
597 buffer for each step were described previously (*47, 48, 60*). The MTPs was assembled on glass
598 slides and ready for use.

599 The $CD8^+$ OT-I cells were injected into the image chamber, allowed to settle and spread
600 on the glass surface for 20 min, and imaged for 30 min with a PerkinElmer confocal microscope
601 with TIRF mode (Hamamatsu sCMOS detector, Nikon Ti-E Microscope, 60× 1.49 TIRF oil
602 objective). The Reflection interference contrast microscopy (RICM) image of a cell appeared as a
603 dark area which was defined as the cell-surface contact area. The tension signal of a cell was
604 measured as the mean Cy3B fluorescence intensity (FI) observed in the total internal reflection
605 fluorescence (TIRF) mode. It was calculated by subtracting the surrounding background level FI
606 from the original contact area FI, and averaging over the spreading area, except for the negative
607 control in which the signal was normalized by the cell size detected on the bright field image, since
608 no detectable cell-surface contact was formed.

609 **Microfluidic cell trap real-time calcium flux analysis**

610 The microfluidic cell trap arrays have previously been described (*54*). Briefly, a layer of
611 polydimethylsiloxane (PDMS) (10:1) was poured on the previously designed and fabricated 8-μm
612 master mold, vacuumed overnight for debubbling, and baked at 70 ºC for 2 h before being peeled
613 off from the mold, cut out and punched the inlet and outlet holes for individual devices. For each
614 PDMS block, the side with micro-channels was treated with oxygen plasma to let it firmly bond
615 to a coverslip. The device was completed by connecting tygon tubing to the inlet and outlet on the
616 PDMS. To functionalize the inner surface to be contacted by cells, the devices were washed with

617 PBS, coated in turn with biotin-BSA for 1 h, streptavidin for 30 min, and biotinylated ligand (0.2
618 mg/ml) for 30 min at room temperature. To avoid unwanted transient stimulation of cells bumping
619 into the coated surface and inlet filter pillars before entering the trapping zone, the inlet channels
620 and filter was blocked with BSA during the biotin-BSA coating step, so the ligand would not be
621 coated to these areas. The device was washed between each coating step by perfusing PBS.

622 $CD8^+$ T cells were loaded with 5 μM of Fluo-4, AM calcium indicator (Thermo Fisher
623 F14201) at 37 ºC for 30 min. Calcium indicator loaded cells at $2 \times 10^6$/ml in the imaging buffer
624 (Hanks' Balanced Salt Solution, or HBSS, with calcium/magnesium and 2% FBS, passed through
625 a 0.45 μm filter) were stabilized for another 30 min at 37 ºC. Cell suspension was aspirated into
626 10 μl pipettor tip and added into the microfluidic device through the inlet. To test the calcium
627 response to soluble factors, calcium indicator-loaded $CD8^+$ T cells were first trapped in the device
628 wells, followed by perfusion of the soluble stimulator. The cell trapping and calcium signaling
629 process was recorded using a PerkinElmer confocal microscope system (Hamamatsu EM-CCD
630 detector, Nikon Ti-E Microscope, 20× 0.75 Air Objective, LiveCell temperature control incubator).
631 The fluorescent signal was recorded continuously for 10 min at 2 frame per sec (fps) for the first
632 5 min and 1 fps for the rest time. Snap shots of bright field images were taken before and after the
633 10 min recording for the device and cell trap quality control. The experiments were performed at
634 37 ºC.

635 Single-cell real-time calcium intensity was analyzed using fluorescent time series data
636 stack. The analysis was similar to those described previously in principle, with the current version
637 of program written in Fiji in house (available upon request). Briefly, the moment that a cell falls
638 into the cell trap is defined as time zero for this cell. The program generates a mask over this cell

639 and the MFI of this mask is tracked in the following frames. This analysis was applied to all cells
640 appeared in the field of view, and then the background FI was subtracted from the MFI. The
641 calcium signal level vs. time sequences for different cells were then realigned at time zero for
642 display and sorting.

643 **Synthetic antigen system**

644 Pyridyl-disulfide functionalized nanoparticles were prepared as previously described (*30, 32, 61*).
645 Cysteine-modified SIINFEKL (CSIINFEKL) was dissolved in MilliQ water at 1 mg/mL and added
646 1:1 to 40 mg/mL PDS-NP. The disulfide displacement reaction proceeded overnight at room
647 temperature with stirring after which SIINFEKL conjugated NP were separated from unreacted
648 peptide by size exclusion chromatography using a CL-6B column. Fractions containing peptide
649 were identified by reacting with fluorescamine, and PEG-containing fractions (NPs) were
650 determined using an iodine assay. Fractions containing CSIINFEKL-NP (Ag-NP) were combined
651 and concentrated to the appropriate dose using 30 kDa MWCO spin filters and sterilized by
652 filtration through a 0.22 µm syringe filter. In select experiments, NPs were reacted with maleimide-
653 AlexaFluor647 or maleimide-AlexaFluor700 during synthesis to render the NP fluorescent (*29-*
654 *32*). Ag-, AF647-, or AF700-NP in sterile saline were injected intradermally in the center of the
655 tumor or into the dermal layer of the skin (non-tumor-bearing animals) of C57Bl/6 mice.

656 ***Ex vivo* Restimulation**

657 After cell isolation (as above, in flow cytometry), 30% of LN samples, 5% of spleen samples, or
658 5% of tumor cells were plated in a sterile 96-well U-bottom plate. 1 µg/mL SIINFEKL peptide in
659 200 µL IMDM media with 10% heat-inactivated FBS and 0.05 mM betamercaptoethanol (Sigma-

660 Aldrich) were added to each sample and incubated for a total of 6 h at 37 ºC with 5% $CO_2$. Three
661 hours into the incubation period, 50 µg/mL Brefeldin A (Sigma-Aldrich) was added to each sample.
662 Cells were washed and stained for flow cytometry as above.

663 **Imaging by In Vivo Imaging System (IVIS)**

664 Animals were injected intradermally in the left dorsal skin with AF647 conjugated NP as described
665 above. 24 h after NP injection, animals were sacrificed via $CO_2$ asphyxiation in accordance with
666 AVMA and local IACUC guidelines. Animals were dissected to expose axillary and brachial LNs
667 and imaged using a Perkins Elmer IVIS Spectrum CT (Waltham, MA). LNs were then dissected
668 and placed on black plastic and imaged using a Perkin Elmer IVIS Spectrum CT.

669 **Tumor Resection**

670 Animals were anesthetized using isoflurane in oxygen, and then given 1 mg/kg sustained release
671 Buprenorphine and 5 mg/kg ketoprofen via intraperitoneal injection as analgesics. The animals
672 were placed on a warming bed and a sterile, fenestrated drape, placed to expose only the tumor
673 and surrounding skin. Povidone-iodine was applied to the skin three times to sterilize the surgical
674 area. Sterile scissors were used to excise and remove the tumor, and sterile wound clips used to
675 close the wound. The animal was monitored throughout recovery and returned to the cage. Animals
676 were monitored every other day to ensure well-being and examine for infection or irritation
677 surrounding the surgical site. Wound clips were removed 10 days post-surgery. All procedures
678 were in accordance with AVMA and local IACUC guidelines.

679 **Statistical analysis**

Data are presented as the mean accompanied by SEM or SD and statistics were calculated using Graphpad Prism 6, 7, and 8 software (Graphpad Software, Inc., La Jolla, CA, USA). Statistical significance was defined as $p<0.05$, 0.01, 0.05, and 0.001 respectively, unless otherwise specified.

**Acknowledgement**

We thank B. Liu, Z. Li, and Y. Chen for contributing to the feasibility studies at the initial stage of this project. This work was supported by NIH grants U01CA214354, R01CA207619, T32GM008433, and T32EB021962. M.P.M. was supported by a National Science Foundation Graduate Research Fellowship.

**Author Contributions**

C.Z. and S.N.T. conceived and supervised the project; Z.Y., M.J.O., J.L., F.Z., P.J., K.B, C.G., M.N.R., L.C., S. R.-C., N.A.R., M.P.M, and D.M.F. performed experiments and analyzed data; K.L. developed image analysis program; H.L. provided specialized devices; C.Z., S.N.T., Z.Y., and M.J.O. wrote the paper.

693 REFERENCES
694


695 1. V. G. Brichard, D. Lejeune, GSK's antigen-specific cancer immunotherapy programme: pilot results leading
696 to Phase III clinical development. *Vaccine* **25**, B61-B71 (2007).

697 2. F. Azimi *et al.*, Tumor-Infiltrating Lymphocyte Grade Is an Independent Predictor of Sentinel Lymph Node
698 Status and Survival in Patients With Cutaneous Melanoma. *Journal of Clinical Oncology* **30**, 2678-2683
699 (2012).

700 3. R. J. Sullivan *et al.*, An update on the Society for Immunotherapy of Cancer consensus statement on tumor
701 immunotherapy for the treatment of cutaneous melanoma: version 2.0. *Journal for immunotherapy of*
702 *cancer* **6**, 1-23 (2018).

703 4. T. F. Gajewski, Failure at the effector phase: immune barriers at the level of the melanoma tumor
704 microenvironment. *Clinical Cancer Research* **13**, 5256-5261 (2007).

705 5. S. Spranger *et al.*, Up-regulation of PD-L1, IDO, and T(regs) in the melanoma tumor microenvironment is
706 driven by CD8(+) T cells. *Sci Transl Med* **5**, 200ra116 (2013).

707 6. Q. Chen, P. Hersey, MHC‐restricted responses of CD8+ and CD4+ T‐cell clones from regional lymph nodes
708 of melanoma patients. *International journal of cancer* **51**, 218-224 (1992).

709 7. I. E. Brown, C. Blank, J. Kline, A. K. Kacha, T. F. Gajewski, Homeostatic proliferation as an isolated variable
710 reverses CD8+ T cell anergy and promotes tumor rejection. *The Journal of Immunology* **177**, 4521-4529
711 (2006).

712 8. Y. Zheng *et al.*, In vivo targeting of adoptively transferred T-cells with antibody- and cytokine-conjugated
713 liposomes. *J Control Release* **172**, 426-435 (2013).

714 9. S. Krishna *et al.*, Stem-like CD8 T cells mediate response of adoptive cell immunotherapy against human
715 cancer. *Science* **370**, 1328-1334 (2020).

716 10. D. T. Alexandrescu *et al.*, Immunotherapy for melanoma: current status and perspectives. *J Immunother* **33**,
717 570-590 (2010).

718 11. J. Naidoo, D. B. Page, J. D. Wolchok, Immune modulation for cancer therapy. *Br J Cancer* **111**, 2214-2219
719 (2014).

720 12. O. Hamid *et al.*, Safety and tumor responses with lambrolizumab (anti-PD-1) in melanoma. *N Engl J Med*
721 **369**, 134-144 (2013).

722 13. S. L. Topalian *et al.*, Survival, durable tumor remission, and long-term safety in patients with advanced
723 melanoma receiving nivolumab. *J Clin Oncol* **32**, 1020-1030 (2014).

724 14. C. Kumpers *et al.*, Immune Cell Infiltration of the Primary Tumor, Not PD-L1 Status, Is Associated With
725 Improved Response to Checkpoint Inhibition in Metastatic Melanoma. *Front Med (Lausanne)* **6**, 27 (2019).

726 15. P. C. Tumeh *et al.*, PD-1 blockade induces responses by inhibiting adaptive immune resistance. *Nature* **515**,
727 568-571 (2014).

728 16. S. Zhong *et al.*, T-cell receptor affinity and avidity defines antitumor response and autoimmunity in T-cell
729 immunotherapy. *Proceedings of the National Academy of Sciences of the United States of America* **110**,
730 6973-6978 (2013).

731 17. J. Huang *et al.*, The kinetics of two-dimensional TCR and pMHC interactions determine T-cell
732 responsiveness. *Nature* **464**, 932-936 (2010).

733 18. B. Liu *et al.*, 2D TCR-pMHC-CD8 kinetics determines T-cell responses in a self-antigen-specific TCR system.
734 *Eur J Immunol* **44**, 239-250 (2014).

735 19. J. Hong *et al.*, Force-Regulated In Situ TCR-Peptide-Bound MHC Class II Kinetics Determine Functions of
736 CD4+ T Cells. *J Immunol* **195**, 3557-3564 (2015).

737 20. D. K. Cole *et al.*, Hotspot autoimmune T cell receptor binding underlies pathogen and insulin peptide cross-
738 reactivity. *The Journal of clinical investigation* **126**, 2191-2204 (2016).

739 21. J. J. Sabatino Jr, J. Huang, C. Zhu, B. D. Evavold, High prevalence of low affinity peptide–MHC II tetramer–
740 negative effectors during polyclonal CD4+ T cell responses. *Journal of Experimental Medicine* **208**, 81-90
741 (2011).

742 22. J. J. Adams *et al.*, T cell receptor signaling is limited by docking geometry to peptide-major histocompatibility
743 complex. *Immunity* **35**, 681-693 (2011).

744 23. J. B. Huppa *et al.*, TCR-peptide-MHC interactions in situ show accelerated kinetics and increased affinity.
745 *Nature* **463**, 963-967 (2010).

746 24. B. Liu *et al.*, The cellular environment regulates in situ kinetics of T-cell receptor interaction with peptide
747 major histocompatibility complex. *Eur J Immunol* **45**, 2099-2110 (2015).

748 25. Y. J. Seo, P. Jothikumar, M. S. Suthar, C. Zhu, A. Grakoui, Local Cellular and Cytokine Cues in the Spleen
749 Regulate In Situ T Cell Receptor Affinity, Function, and Fate of CD8(+) T Cells. *Immunity* **45**, 988-998 (2016).

750 26. M. J. O'Melia *et al.*, Quality of CD8(+) T cell immunity evoked in lymph nodes is compartmentalized by route
751 of antigen transport and functional in tumor context. *Sci Adv* **6**, (2020).

752 27. S. N. Thomas *et al.*, Engineering complement activation on polypropylene sulfide vaccine nanoparticles.
753 *Biomaterials* **32**, 2194-2203 (2011).

754 28. S. N. Thomas, E. Vokali, A. W. Lund, J. A. Hubbell, M. A. Swartz, Targeting the tumor-draining lymph node
755 with adjuvanted nanoparticles reshapes the anti-tumor immune response. *Biomaterials* **35**, 814-824 (2014).

756 29. A. Schudel, L. F. Sestito, S. N. Thomas, Winner of the society for biomaterials young investigator award for
757 the annual meeting of the society for biomaterials, April 11-14, 2018, Atlanta, GA: S-nitrosated
758 poly(propylene sulfide) nanoparticles for enhanced nitric oxide delivery to lymphatic tissues. *J Biomed*
759 *Mater Res A* **106**, 1463-1475 (2018).

760 30. A. Schudel *et al.*, Programmable multistage drug delivery to lymph nodes. *Nat Nanotechnol* **15**, 491-499
761 (2020).

762 31. L. F. Sestito, S. N. Thomas, Lymph-directed nitric oxide increases immune cell access to lymph-borne
763 nanoscale solutes. *Biomaterials* **265**, 120411 (2021).

764 32. D. M. Francis *et al.*, Drug-eluting immune checkpoint blockade antibody-nanoparticle conjugate enhances
765 locoregional and systemic combination cancer immunotherapy through T lymphocyte targeting.
766 *Biomaterials* **279**, 121184 (2021).

767 33. S. M. Kaech, R. Ahmed, Memory CD8+ T cell differentiation: initial antigen encounter triggers a
768 developmental program in naive cells. *Nat Immunol* **2**, 415-422 (2001).

769 34. A. H. Sharpe, K. E. Pauken, The diverse functions of the PD1 inhibitory pathway. *Nat Rev Immunol* **18**, 153-
770 167 (2018).

771 35. R. Sackstein, T. Schatton, S. R. Barthel, T-lymphocyte homing: an underappreciated yet critical hurdle for
772 successful cancer immunotherapy. *Lab Invest* **97**, 669-697 (2017).

773 36. S. N. Thomas, E. Vokali, A. W. Lund, J. A. Hubbell, M. A. Swartz, Targeting the tumor-draining lymph node
774 with adjuvanted nanoparticles reshapes the anti-tumor immune response. *Biomaterials* **35**, 814-824 (2014).

775 37. D. M. Francis *et al.*, Blockade of immune checkpoints in lymph nodes through locoregional delivery
776 augments cancer immunotherapy. *Science Translational Medicine* **12**, (2020).

777 38. N. A. Rohner, S. N. Thomas, Flexible macromolecule versus rigid particle retention in the injected skin and
778 accumulation in draining lymph nodes are differentially influenced by hydrodynamic size. *ACS biomaterials*
779 *science & engineering* **3**, 153-159 (2017).

780 39. S. E. Chesla, P. Selvaraj, C. Zhu, Measuring two-dimensional receptor-ligand binding kinetics by
781 micropipette. *Biophysical journal* **75**, 1553-1572 (1998).

782 40. Q. Ge *et al.*, Development of CD4+ T cells expressing a nominally MHC class I-restricted T cell receptor by
783 two different mechanisms. *Proc Natl Acad Sci U S A* **103**, 1822-1827 (2006).

784 41. N. Jiang *et al.*, Two-stage cooperative T cell receptor-peptide major histocompatibility complex-CD8
785 trimolecular interactions amplify antigen discrimination. *Immunity* **34**, 13-23 (2011).

786 42. M. N. Rushdi *et al.*, Cooperative binding of TCR and CD4 to pMHC enhances TCR sensitivity. *bioRxiv*,
787 https://www.biorxiv.org/content/10.1101/2021.1111.1122.469547v469541 (2022).

788 43. M. Pickup, S. Novitskiy, H. L. Moses, The roles of TGFβ in the tumour microenvironment. *Nature Reviews*
789 *Cancer* **13**, 788-799 (2013).

790 44. Y. Y. Wan, R. A. Flavell, 'Yin-Yang' functions of transforming growth factor-beta and T regulatory cells in
791 immune regulation. *Immunol Rev* **220**, 199-213 (2007).

792 45. M. O. Li, R. A. Flavell, TGF-β: a master of all T cell trades. *Cell* **134**, 392-404 (2008).

793 46. M.-L. Chen *et al.*, Regulatory T cells suppress tumor-specific CD8 T cell cytotoxicity through TGF-β signals in
794 vivo. *Proceedings of the National Academy of Sciences* **102**, 419-424 (2005).

795 47. Y. Liu *et al.*, DNA-based nanoparticle tension sensors reveal that T-cell receptors transmit defined pN forces
796 to their antigens for enhanced fidelity. *Proc Natl Acad Sci U S A* **113**, 5610-5615 (2016).

797 48. J. Hong *et al.*, A TCR mechanotransduction signaling loop induces negative selection in the thymus. *Nat*
798 *Immunol* **19**, 1379-1390 (2018).

799 49. Y. Liu, K. Galior, V. P. Ma, K. Salaita, Molecular Tension Probes for Imaging Forces at the Cell Surface. *Acc*
800 *Chem Res* **50**, 2915-2924 (2017).

801 50. R. Ma *et al.*, DNA Tension Probes to Map the Transient Piconewton Receptor Forces by Immune Cells.
802 *Journal of visualized experiments : JoVE*, (2021).

803 51. R. Bender, K. Salaita, *Molecular Force Sensors*. (American Chemical Society, 2022).

804 52. Y. Zhang, C. Ge, C. Zhu, K. Salaita, DNA-based digital tension probes reveal integrin forces during early cell
805 adhesion. *Nature communications* **5**, 5167 (2014).

806 53. C. Jurchenko, K. S. Salaita, Lighting Up the Force: Investigating Mechanisms of Mechanotransduction Using
807 Fluorescent Tension Probes. *Molecular and cellular biology* **35**, 2570-2582 (2015).

808 54. K. Chung, C. A. Rivet, M. L. Kemp, H. Lu, Imaging single-cell signaling dynamics with a deterministic high-
809 density single-cell trap array. *Anal Chem* **83**, 7044-7052 (2011).

810 55. A. W. Lund *et al.*, VEGF-C promotes immune tolerance in B16 melanomas and cross-presentation of tumor
811 antigen by lymph node lymphatics. *Cell Rep* **1**, 191-199 (2012).

812 56. M. Binnewies *et al.*, Understanding the tumor immune microenvironment (TIME) for effective therapy. *Nat*
813 *Med* **24**, 541-550 (2018).

814 57. S. P. Kim *et al.*, Adoptive Cellular Therapy with Autologous Tumor-Infiltrating Lymphocytes and T-cell
815 Receptor–Engineered T Cells Targeting Common p53 Neoantigens in Human Solid Tumors. *Cancer*
816 *immunology research* **10**, 932-946 (2022).

817 58. C. U. Blank *et al.*, Defining 'T cell exhaustion'. *Nature Reviews Immunology* **19**, 665-674 (2019).

818 59. S. Nagaraj *et al.*, Altered recognition of antigen is a mechanism of CD8+ T cell tolerance in cancer. *Nat Med*
819 **13**, 828-835 (2007).

820 60. R. Ma *et al.*, DNA probes that store mechanical information reveal transient piconewton forces applied by
821 T cells. *Proc Natl Acad Sci U S A* **116**, 16949-16954 (2019).

822 61. A. J. van der Vlies, C. P. O'Neil, U. Hasegawa, N. Hammond, J. A. Hubbell, Synthesis of pyridyl disulfide-
823 functionalized nanoparticles for conjugating thiol-containing small molecules, peptides, and proteins.
824 *Bioconjug Chem* **21**, 653-662 (2010).

825

826 **Figure legends**

827 **Fig. 1. Functionally impaired antigen-specific CD8$^+$ T cell responses in the TME. (A)**
828 Animal models used in (*B*)-(*F*). *Left*, B16F10 melanoma cells were intradermally injected into
829 the lateral dorsal skin of C57BL/6 mice at d-8. Ag-NPs were administered at d-1 into the tumor.
830 *Right*, Ag-NPs were administered into the tumor-naïve lateral dorsal skin at d-1. *Both*, at d0,
831 B16F10-OVA melanoma cells were injected into the contralateral dorsal skin. Primary
832 melanomas were resected at d2 and tumor growth as well as animal survival were monitored. **(B)**
833 IVIS image of AF647 signal 24 h post AF647-labelled NP administration i.d. into the lateral
834 dorsal skin. *Left*, NP injection site (white arrow) and dLN (green circle). *Right*, dLN and NdLN
835 after excision. **(C)** Schematic of the Ag-NPs. **(D)** Number of CD3$^-$ cells positively stained by a
836 mAb against SIINFEKL:H2-K$^b$ (clone 25D1.16) 24 h after *in vitro* coincubation of SIINFEKL
837 with splenocytes. Each point represents a technical replicate. Mean ± SD (lines). **(E, F)** Mean ±
838 SEM (n=5) of size of contralateral (secondary) tumor (*E*) and animal survival (*F*) after Ag-NP
839 challenge in the tumor (red) or naïve skin (gray), corresponding to the model cohorts depicted in
840 (*A*). **(G)** Animal model used in (*H*)-(*N*). *Left*, B16F10 melanoma cells were injected into
841 CD45.1$^+$ C57BL/6 recipient mice at d-7. *Left and right*, CD8$^+$ T cells isolated from the spleens of
842 CD45.2$^+$ OT-I donor mice were adoptive transferred at d-1 and Ag-NPs or saline was
843 administered i.t. into B16F10 bearing animals (Tumor-bearing) or the naïve skin (Naïve) at d0.
844 At d3 the donor cells were harvested from recipient mice and analyzed. **(H)** Number of CD45.2$^+$
845 OT-I cells in each proliferative generation in response to *in vivo* challenge with Ag-NP in the
846 tumor (red) of the tumor-bearing animals and the naïve skin of the control animals (gray). Data
847 represents mean ± SEM. n=5. **(I-K)** Comparison of frequency (*I*) and number (*J*, *K*) of indicated
848 phenotypic marker expressing CD45.2$^+$ populations between cells harvested from the tumor (*i, j*)
849 or the LNs draining the tumor (*K*) of the tumor-bearing animals (red) and from naïve skin (*I, J*)
850 or the LNs draining the naïve skin (*K*) of the control animals (gray) after *in vivo* Ag challenge.
851 Each point represents individual animal. Data represent mean ± SEM. n=5. **(L, M)** Comparison
852 of anti-PD-1 mAb fluorescence intensity (FI) profile using representative histogram from donor
853 cells from an individual animal from each group (*L*) and mean ± SEM (n=5) of mean FI (MFI) of
854 PD-1$^+$subpopulation in each proliferative generation (*M*) between CD45.2$^+$ cells harvested from
855 the LNs draining the tumor of the tumor-bearing animals (red) or the naïve skin of the control
856 animals (gray). **(N)** Frequency of PD-1$^+$ and CD25$^+$ cells over CD45.2$^+$ population in the spleen
857 of tumor-bearing (red) or tumor-lacking (gray) animals after *in vivo* Ag challenge. Each point
858 represents individual animal. Data represent mean ± SEM. n=5. "*" indicates significance by
859 two-way ANOVA with Tukey's post-hoc test; "#" indicates significance compared to theoretical
860 value of 1.0 by one-sample t-test; "^" indicates significance by Log-rank (Mantel-Cox) test;
861 $ indicates significance by repeat measures ANOVA; Tumor growth and survival experiments in
862 (*E*)-(*F*) are representative of two independent experiments.

863

864 **Fig. 2. Lowered T cell activation response and TCR–pMHC 2D affinity of CD8$^+$ T cells**
865 **recovered from tumors and TdLNs. (A)** Animal models used in (*B*)-(*D*). *Left*, CD45.1$^+$
866 C57BL/6J recipients were implanted with B16F10 tumor on d-7. *Left and right*, splenic CD8$^+$ T

867 cells from CD45.2$^+$ OT-I mice adoptively transferred into recipient animals d0 and donor cells
868 were harvested d3. **(B-D)** Activation and function in response to *ex vivo* SIINFEKL challenge of
869 CD45.2$^+$ donor cells harvested from tumor vs naïve skin (*B*), tumor- vs naïve-dLNs (*C*), and
870 spleens (*D*) of tumor-bearing (red) vs -naïve (gray) animals were analyzed by for the indicated
871 phenotypical markers. Each point represents data from one individual animal. Data represents
872 mean ± SEM. Representative results of two independent experiments with n≥3. **(E)** Animal
873 model used in (*G*). CD45.1$^+$ C57BL/6J recipients that were tumor-naïve (*right*) or had just been
874 implanted with B16F10 tumors (*left*) were adoptively transferred with splenic CD8$^+$ T cells from
875 CD45.2$^+$ OT-I mice on d0. At d7, CD45.2$^+$ donor cells were isolated from recipients' TdLNs and
876 spleen for binding analysis. **(F)** Schematic of micropipette adhesion frequency (MAF) assay. A
877 micropipette-aspirated RBC coated with SINNFEKL:H2-K$^b$α3A2 (*left*) was driven to repeatedly
878 contact a donor CD8$^+$ T cell expressing OT-I TCR, aspirated by an opposing micropipette
879 (*right*). Adhesion mediated by TCR–pMHC interaction, if occurred, was detected visually by
880 RBC elongation. An adhesion frequency ($P_a$ = # of adhesions/# of total contacts) was evaluated
881 from 50 times of repeated 2-s contacts between a RBC–T cell pair from which an effective 2D
882 affinity $A_cK_a = -\ln(1 - P_a)/(m_{TCR}m_{pMHC})$ was calculated. Here $A_c$ is the constant contact area and
883 $m_{TCR}$ and $m_{pMHC}$ are the respective densities of TCR and pMHC measured separately by FACS.
884 **(G)** Comparison of TCR–pMHC 2D affinities measured from indicated conditions. 2D affinity
885 of each compartment was divided by the mean $A_cK_a$ value of T cells from the spleen of the same
886 animal (to normalize inter-animal variations). Results shown in (*B*)-(*D*) were from n= 3-5 mice;
887 "*" indicates significance by two-way ANOVA with Tukey's post-hoc test. Data in (*G*) are
888 presented as mean (line) ± 75/25% (boxes) and max/min (whiskers) of pooled measurements
889 from two independent sets of experiments in order to test sufficient number (24-31) of T cells per
890 condition to ensure reliable statistical comparisons (Mann-Whitney test). ***p<0.001, ns
891 indicates p≥0.05.

892

893 **Fig. 3. Suppressed TCR antigen recognition by tumor and TdLN-localized CD8$^+$ T cells.**
894 **(A)** Animal model used in (*B*)-(*G*) in which CD8$^+$ T cells were isolated from indicated tissues of
895 B16F10 tumor-bearing OT-I mice at indicated timepoints for analysis. **(B)** Comparison of OT-I
896 TCR–SIINFEKL:H2-K$^b$α3A2 2D affinities evaluated using CD8$^+$ T cells from the indicated
897 tissues. **(C)** Comparison of CD8–VSV:H2-K$^b$ 2D affinities evaluated using CD8$^+$ T cells from
898 TdLN and NdLN of the same OT-I mouse. **(D)** Comparison between adhesion frequencies of
899 RBCs bearing anti-TCR antibody and CD8$^+$ T cells from TdLN and NdLN of the same OT-I
900 animal. **(E)** Comparison of average numbers of bonds per contact from OT-I CD8$^+$ T cells–
901 SIINFEKL:H2-K$^b$ interaction, calculated from adhesion frequencies by $\langle n \rangle = -\ln(1 - P_a)$,
902 normalized by the densities of the TCR ($m_{TCR}$) and pMHC ($m_{pMHC}$), evaluated using CD8$^+$ T
903 cells from TdLN and NdLN. Since $\langle n \rangle/(m_{TCR}m_{pMHC})$ is the effective 2D affinity $A_cK_{a,TCR}$ of the
904 TCR–pMHC bonds in the absence of CD8 binding, the 1 log higher $\langle n \rangle/(m_{TCR}m_{pMHC})$ values
905 observed here (which include not only TCR–pMHC bonds but also TCR–pMHC–CD8 and
906 CD8–MHC bonds) than the corresponding values in (*B*) (which include only TCR–pMHC
907 bonds) indicate that the trimolecular bonds greatly outnumber the two bimolecular bonds. **(F)**
908 Comparison of 2D affinities of CD8 for pre-formed TCR–pMHC complex, $K_a^*{}_{,CD8}$ =

909 [$<n>/(A_c K_{a,TCR} m_{TCR} m_{pMHC}) - 1]/m_{CD8}$, evaluated using $CD8^+$ T cells from TdLN and NdLN of
910 the same OT-1 mouse. The calculation of $K_a^*{}_{,CD8}$ used the CD8 site density ($m_{CD8}$) measured
911 from flow cytometry, and the data from (*B*) and (*E*) by subtracting the contribution of the TCR–
912 pMHC bonds from the total bonds. The contribution of CD8–MHC bond was neglected since the
913 CD8–MHC affinity is ~500-fold smaller than the TCR–pMHC affinity. **(G)** Same as (*B*) except
914 that the experiments were done 3- and 11-days post tumor injection for only two tissue sources.
915 Data are presented as mean (line) ± 75/25% (boxes) and max/min (whiskers) of pooled
916 measurements from 2-6 independent experiments in order to test sufficient number (4-27) of T
917 cells per condition to ensure reliable statistical comparisons (Mann-Whitney test).

918

919 **Fig. 4. TGF-β inhibition eliminates differential TCR–pMHC 2D affinities between $CD8^+$ T**
920 **cells from TdLNs vs NdLNs. (A)** Animal model used in (*B*). B16F10 tumor-bearing OT-I mice
921 were treated with TGF-β inhibitor or DMSO as control in d4, d5, and d6 post tumor
922 implantation. **(B)** Comparisons of OT-I TCR–SIINFEKL:H2-$K^b$α3A2 2D affinities evaluated
923 using $CD8^+$ T cells from TdLN and NdLN of mice treated with TGF-β inhibitor (*left*) or DMSO
924 (*right*). Data are presented and statistically analyzed the same way as Fig. 3.

925

926 **Fig. 5. Cell spreading and pulling on antigen pMHC is diminished for $CD8^+$ T cells isolated**
927 **from TdLNs. (A)** Schematic of DNA-based MTP, consisting of a Cy3B-quencher pair flanking
928 a DNA hairpin to unfold at >4.7 pN forces. One end presents a pMHC or antibody to the TCR
929 and/or CD8 and the other end is linked to the cover glass *via* a gold nanoparticle to further
930 quench the fluorophore. A >4.7 pN force exerted on the pMHC or antibody by the cell unfolds
931 the DNA-hairpin and de-quenches the Cy3B to yield a fluorescent signal. **(B)** Representative
932 images of $CD8^+$ T cells from TdLNs or NdLNs of OT-I mice 7 days post tumor implantation
933 placed on glass surfaces functionalized with MTPs tagged by SIINFEKL:H2-$K^b$, anti-TCR or
934 BSA viewed 10 min after cell seeding by bright-field (top row), RICM (middle row) and TIRF
935 (bottom row). **(C, D)** Quantification of the spreading area (middle row in *B*) (*C*) and mean
936 fluorescence intensity (MFI) of the force signal (bottom row in *B*) (*D*) using a large number of
937 cells. Points, mean (line) ± 75/25% (boxes) and max/min (whiskers) from a representative
938 experiment that repeated three times. Analyzed $CD8^+$ T cells were recovered from TdLNs vs
939 NdLNs of d7 B16F10 melanoma-bearing animals as depicted in Fig. 3a. ****$p \leq 0.0001$, *$p \leq 0.05$,
940 n.s.: $p \geq 0.05$.

941

942 **Fig. 6. TdLN suppressed calcium response of $CD8^+$ T cells to antigen stimulation. (A)**
943 Bright-field (*top*) and fluorescence (*bottom*) photomicrographs of the microfluidic cell trap array
944 device used for the real-time calcium flux experiments. **(B)** Heatmaps of single-cell real-time
945 Fluo-4 fluorescence intensity (FI) of the $CD8^+$ T cells from TdLN (*top row*) or NdLN (*bottom*
946 *row*) of an OT-I mouse in d7 post tumor implantation (representative results from three
947 independent experiments). The inner surface of the cell traps was coated with either BSA (*left*
948 *column*) or SIINFEKL:H2-$K^b$ (*right column*). For each cell, time zero was the moment when the

949 cell was trapped by a well, and each streak indicates the real-time Fluo-4 intensity for a tracked
950 cell. Streaks were ranked in ascending order of cumulated FI over 300 sec. **(C)** Mean FI of the
951 real-time calcium flux over all the cells from (*B*). **(D)** Cumulated FI over 300 s for each cell from
952 (*B*). **(E-G)** Calcium response to perfusion of 1 μM ionomycin of $CD8^+$ T cells from TdLN or
953 NdLN of an OT-I mouse in d7 post tumor implantation (representative results from two
954 independent experiments). Data presentation are parallel to (*B-D*), showing heatmaps (*E*),
955 associated mean FI vs time (*F*) and cumulated calcium intensity (*G*) after ionomycin
956 administration. Analyzed $CD8^+$ T cells were recovered from TdLNs vs NdLNs of d7 B16F10
957 melanoma-bearing animals as depicted in Fig. 3A. Data are presented as mean ± SEM in (*C*) and
958 (*F*), individual cells (points), mean (line) ± 75/25% (boxes) and max/min (whiskers) in (*D*) and
959 (*G*). Statistical comparisons by Mann-Whitney test, ****$p<0.0001$, n.s.: $p\geq0.05$.

960

961 **Fig. 7. TdLN suppressed TCR–pMHC 2D affinity of antigen-experienced $CD8^+$ T cells**
962 **associated with altered profiles of activation and function. (A)** Animal model used in (*B-C*).
963 $CD45.1^+$ C57BL/6J recipients implanted with B16F10 melanoma (Tumor) or left untreated
964 (Naïve) were adoptively transferred with splenic $CD8^+$ T cells from $CD45.2^+$ OT-I mice at d0,
965 immunized with Ag-NP and CpG-NP at d3, and sacrificed at d7 to isolate donor T cells from
966 spleen and TdLNs (for Tumor-bearing mice) or LNs (for Naive mice) for analysis. **(B)**
967 Comparisons of fluorescent histograms of CD44 expression of $CD45.2^+$ (donor) and $CD45.1^+$
968 (endogenous) $CD8^+$ T cells from LNs and spleens in response to vaccination. Representative
969 histogram of one sample from each group. **(C)** Comparisons of OT-I TCR–SIINFEKL:H2-
970 $K^b\alpha3A2$ 2D affinities of $CD8^+$ T cells from spleen and TdLN of tumor-bearing recipients (red)
971 and tumor-lacking recipients (gray), divided by the mean 2D affinity from the spleen of the same
972 animal for each group to normalize variations between animals. Data presented as mean ±
973 75/25% (box) and max/min (whiskers) were pooled from two independent sets of experiments to
974 acquire sufficient number (17-20) of T cells per condition to allow for reliable statistic
975 comparison (Mann-Whitney test). **(D)** Animal model used in (*E*) and (*F*). *Left*, $CD45.1^+$
976 C57BL/6J recipient animals were implanted with B16F10 melanoma at d-3. *Left and right*, donor
977 splenic $CD8^+$ T cells from $CD45.2^+$ OT-I mice were adoptively transferred at d-1, and tumor-
978 bearing (Tumor) or tumor-naïve (Naïve) animals were challenged with Ag-NP at d0 either i.t. or
979 i.d., respectively, and animals were sacrificed at d3 to isolate donor T cells from TdLN and
980 spleen (for tumor-bearing mice) or LN and spleen (for control mice) for analysis. **(E, F)**
981 Comparisons of responses to *ex vivo* restimulated by SIINFEKL of donor cells harvested from
982 TdLN vs LN (*E*) and spleens (*F*) of respective tumor-bearing vs -naïve animals by the number of
983 cells expressing the indicated phenotypical markers. Each point represents data from an
984 individual mouse. Data is the mean ± SEM. n=5. **(G)** Schematic of the model used in (*H*). Donor
985 splenic $CD8^+$ T cells from $CD45.2^+$ OT-I mice were adoptively transferred d-1 into $CD45.1^+$
986 C57BL/6J recipient animals implanted with B16F10-OVA B16F10-OVA tumors on d0. Donor T
987 cells from spleen and TdLNs (for Tumor-bearing mice) or LNs (for Naive mice) were isolated
988 from animals d7 for analysis **(H)** Comparisons of OT-I TCR–SIINFEKL:H-$2K^b\alpha3A2$ 2D
989 affinities of $CD45.2^+CD8^+$ donor T cells harvested from the indicated tissue compartments of the
990 $CD45.1^+$ C57BL/6J recipients bearing B16F10-OVA tumors. n=16-20 T cells pooled from

991 repeated independent experiments. *indicates significance by two-way ANOVA with Tukey's
992 post-hoc test (*E*, *F*), or Mann-Whitney test (*C*, *H*).

993

994 **Supplemental Fig. 1. Tumor growth and immune phenotyping of B16F10 tumor growth in**
995 **C57Bl/6 versus OT-I mice. (A)** Volumes of B16F10 melanomas implanted in C57BL/6J and
996 OT-I animals. **(B)** Identification of dLN by intratumoral injection of AF700-labelled lymph-
997 draining particles (*top, right*) comparing to saline injection (*bottom*). **(C)** Major immune cell
998 subtypes in animals bearing d7 B16F10. **(D-J)** Number of $CD8^+$ T cells (*D*), PD-$1^+CD8^+$ T cells
999 (*E*), $CD25^+CD8^+$ T cells (*F*), $CD4^+$ T cells (*G*), Tregs (*H*), MDSCs (*I*), and PD-$L1^+CD45^+$ cells
1000 (*J*), in naïve, d3, d7, and d11 B16F10 tumors, dLNs, and spleens. "*" indicates difference
1001 between animal type by two-way ANOVA; "^" indicates difference between timepoints in each
1002 animal type (against all other timepoints if not specified). Data represent ± SEM (*A*, *D-J*). n=5.

1003

1004 **Supplemental Fig. 2. Assessment of $CD8^+$ T cells from various tissue compartments of**
1005 **B16F10-bearing (red) and -lacking (gray) OT-I animals. (A)** Ratios of OT-I TCR–
1006 SIINFEKL:H2-$K^b$α3A2 2D affinity of $CD8^+$ T cells from TdLN over that from NdLN in d3, d7
1007 and d11 post tumor implantation. Data are presented as mean ± SD and assessed statistically by
1008 one sample t tests with hypothesis form zero. **(B, C)** TCR expression on $CD8^+$ T cells from
1009 indicated tissue sources in mice bearing (red) or lacking (gray) a d7 tumor, shown as MFI of
1010 saturating concentration staining by an anti-TCR antibody (*B*) and FI histograms (curves) and
1011 MFI (numbers) of saturating concentration staining by SIINFEKL:H-$2K^b$ (*left*) and
1012 SIINFEKL:H-$2K^b$α3A2 tetramers (*right*) (*C*).

1013

## Figure 1

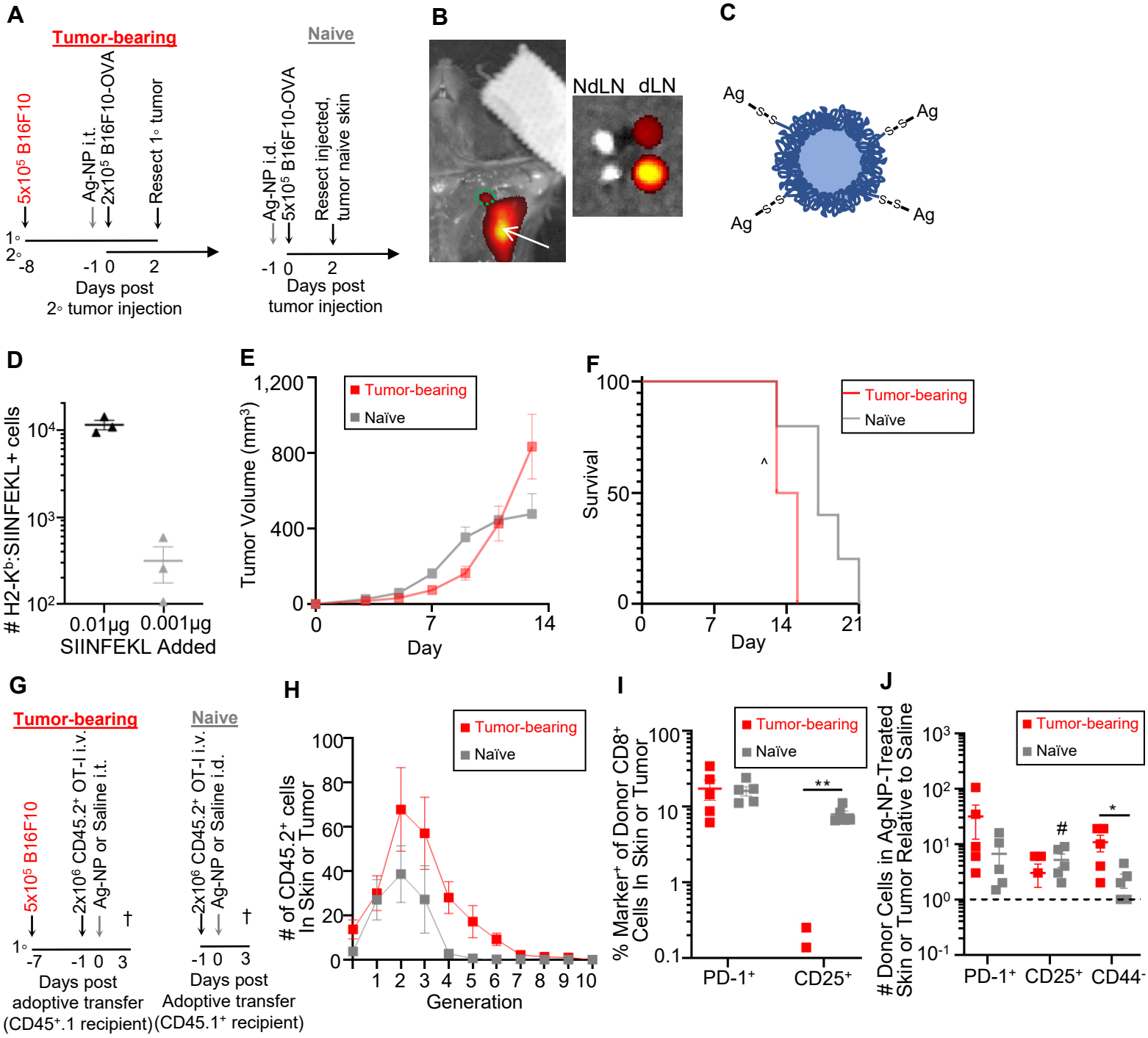
A
Tumor-bearing
5x10^5 B16F10
Ag-NP i.t.
2x10^5 B16F10-OVA
Resect 1° tumor
1°
2°
-8
-1 0 2
Days post
2° tumor injection
Naive
Ag-NP i.d.
5x10^5 B16F10-OVA
Resect injected, tumor naive skin
-1 0 2
Days post
tumor injection
B
NdLN dLN
C
Ag
D
# H2-K^b:SIINFEKL+ cells
0.01μg 0.001μg
SIINFEKL Added
E
Tumor-bearing
Naïve
Tumor Volume (mm^3)
Day
F
Tumor-bearing
Naïve
Survival
Day
G
Tumor-bearing
5x10^5 B16F10
2x10^6 CD45.2^+ OT-I i.v.
Ag-NP or Saline i.t.
†
-7 -1 0 3
Days post
adoptive transfer
(CD45^+.1 recipient)
Naive
2x10^6 CD45.2^+ OT-I i.v.
Ag-NP or Saline i.d.
-1 0 3
Days post
Adoptive transfer
(CD45.1^+ recipient)
H
# of CD45.2^+ cells In Skin or Tumor
Generation
I
% Marker^+ of Donor CD8^+ Cells In Skin or Tumor
PD-1^+
CD25^+
J
# Donor Cells in Ag-NP-Treated Skin or Tumor Relative to Saline
PD-1^+ CD25^+ CD44^-
K
# Marker^+ CD8^+ cells in dLN
Tumor -bearing
Naïve
PD-1^+
CD25^+
L
from LN draining
Ag-NP injection site
Normalized count of Donor CD8^+ T cells
PD-1
M
PD-1^+ CD8^+ dLN cells
PD1 MFI
Generation
N
% Marker^+ of CD8^+ cells In Spleen
PD-1^+
CD25^+

**Figure 2**

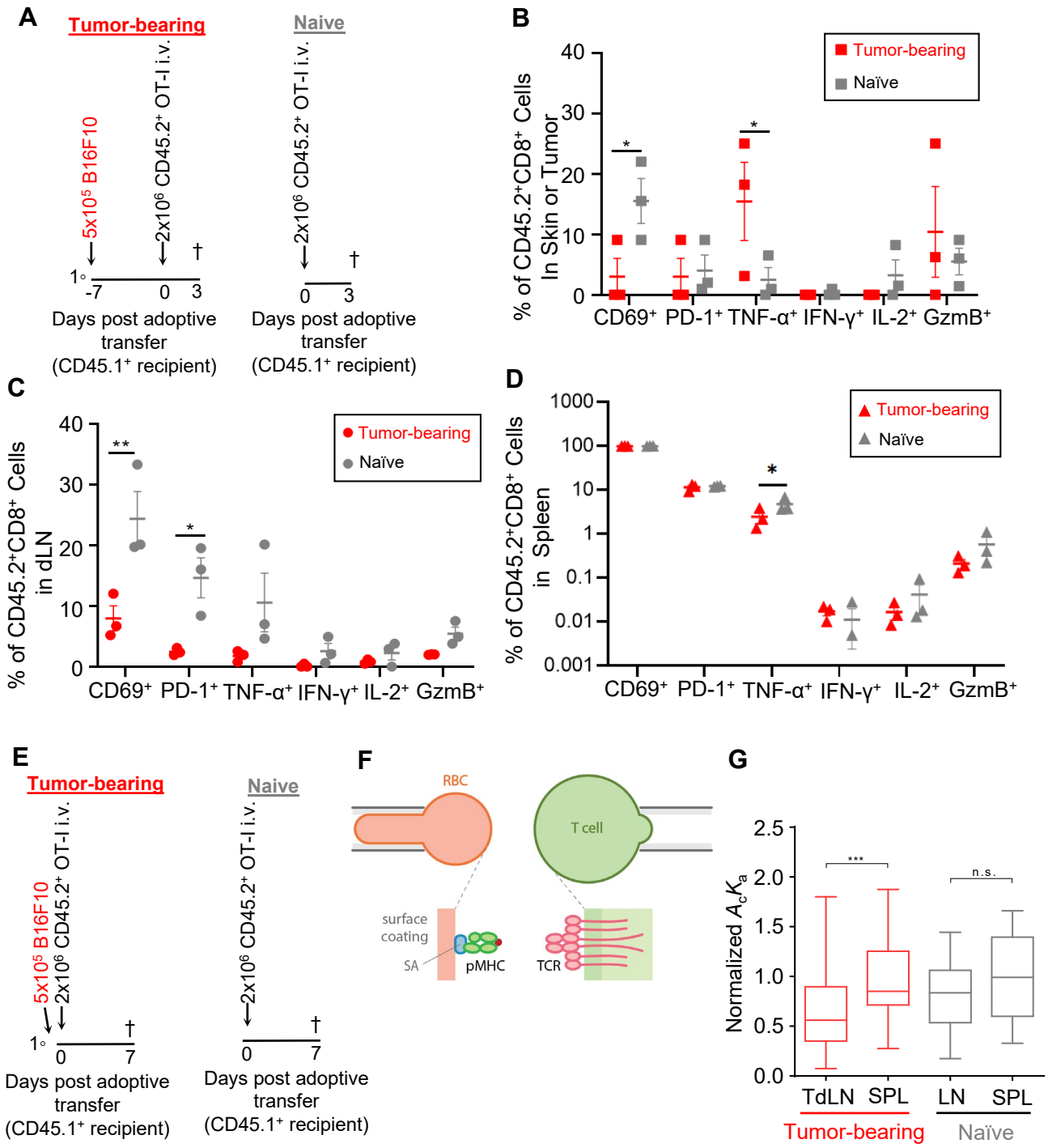
A
Tumor-bearing
Naive
5x10^5 B16F10
2x10^6 CD45.2^+ OT-I i.v.
1°
-7
0
3
†
Days post adoptive transfer (CD45.1^+ recipient)
B
Tumor-bearing
Naïve
% of CD45.2^+CD8^+ Cells In Skin or Tumor
CD69^+ PD-1^+ TNF-α^+ IFN-γ^+ IL-2^+ GzmB^+
C
% of CD45.2^+CD8^+ Cells in dLN
D
% of CD45.2^+CD8^+ Cells in Spleen
E
F
RBC
T cell
surface coating
SA
pMHC
TCR
G
Normalized $A_cK_a$
TdLN
SPL
LN
Tumor-bearing
Naïve
n.s.

**Figure 3**

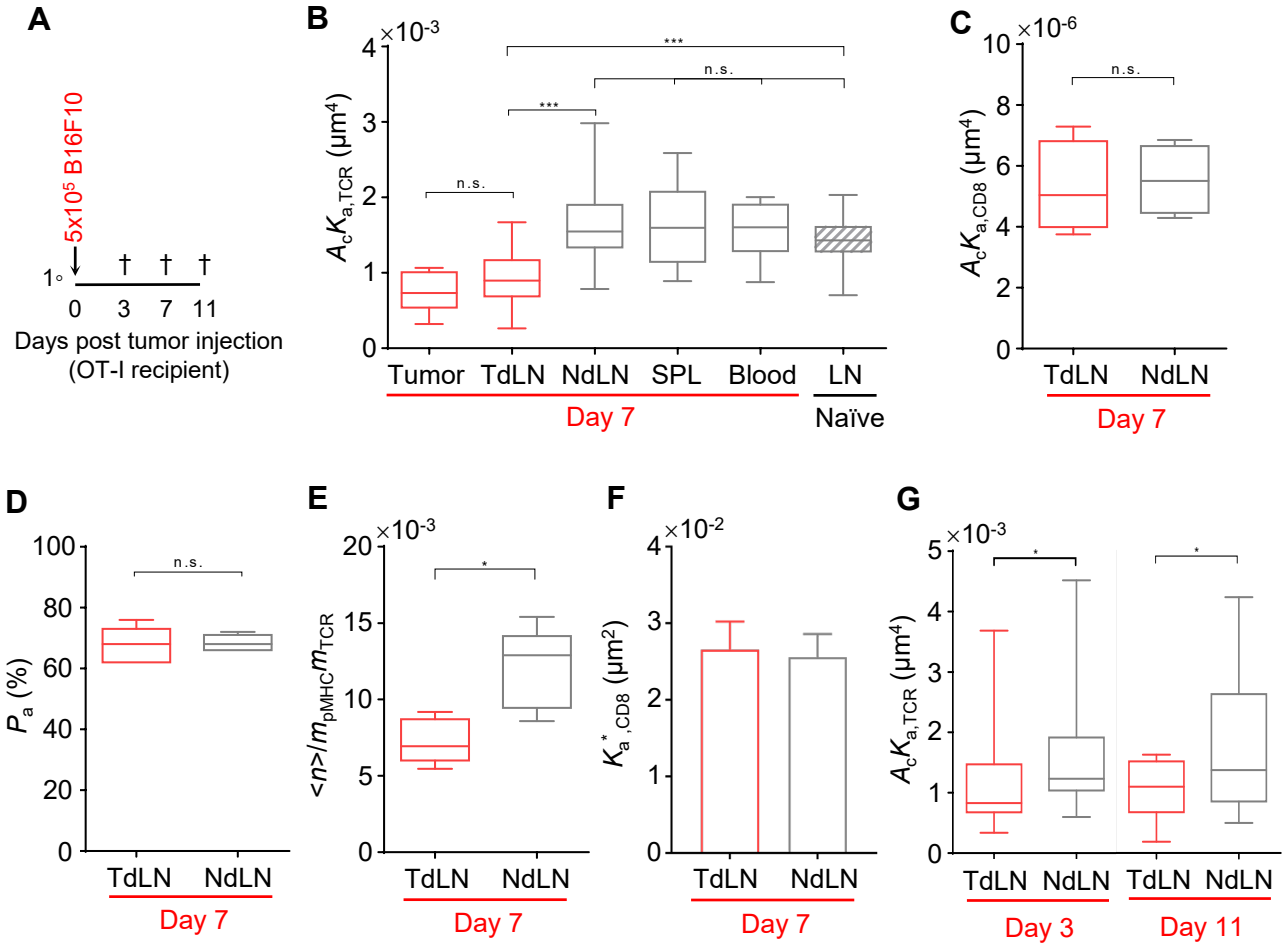
A
5x10^5 B16F10
1°
0 3 7 11
Days post tumor injection
(OT-I recipient)
B
×10^-3
A_cK_a,TCR (μm^4)
n.s.
***
***
n.s.
Tumor TdLN NdLN SPL Blood LN
Day 7
Naïve
C
×10^-6
A_cK_a,CD8 (μm^4)
n.s.
TdLN NdLN
Day 7
D
P_a (%)
n.s.
TdLN NdLN
Day 7
E
×10^-3
<n>/m_pMHC m_TCR
*
TdLN NdLN
Day 7
F
×10^-2
K*_a,CD8 (μm^2)
TdLN NdLN
Day 7
G
×10^-3
A_cK_a,TCR (μm^4)
*
*
TdLN NdLN TdLN NdLN
Day 3 Day 11

**Figure 4**

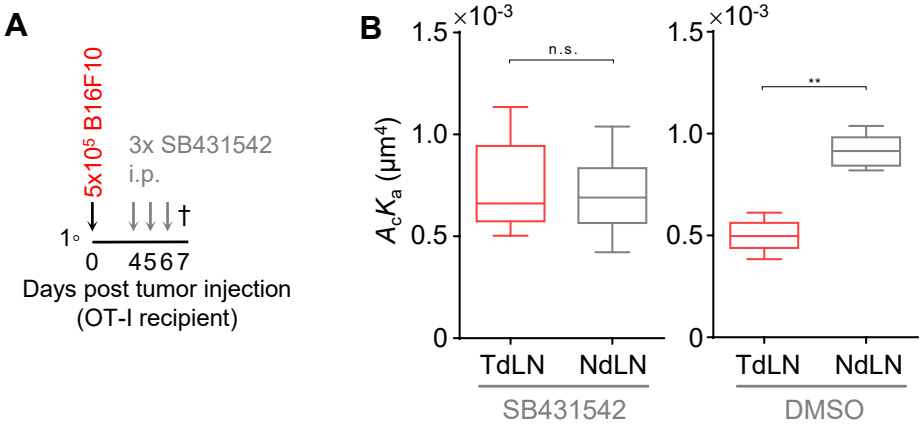
A
5x10^5 B16F10
3x SB431542
i.p.
1°
†
0 4567
Days post tumor injection
(OT-I recipient)
B
×10^-3
1.5
1.0
0.5
0
n.s.
**
A_cK_a (μm^4)
TdLN
NdLN
SB431542
DMSO

**Figure 5**

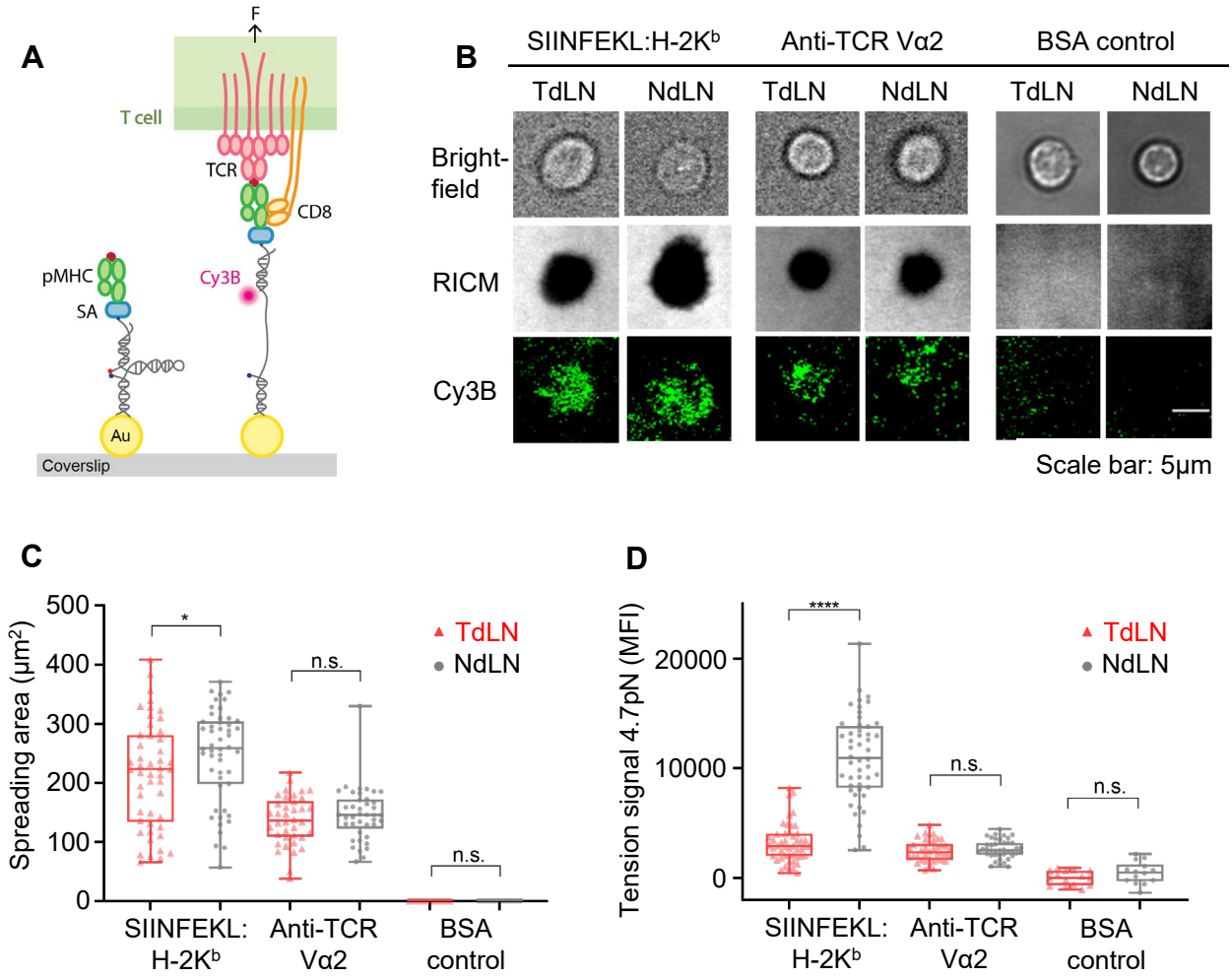
A
F
T cell
TCR
CD8
pMHC
SA
Cy3B
Au
Coverslip
B
SIINFEKL:H-2Kᵇ
Anti-TCR Vα2
BSA control
TdLN
NdLN
Bright-field
RICM
Cy3B
Scale bar: 5μm
C
Spreading area (μm²)
500
400
300
200
100
0
*
n.s.
n.s.
TdLN
NdLN
SIINFEKL: H-2Kᵇ
Anti-TCR Vα2
BSA control
D
Tension signal 4.7pN (MFI)
20000
10000
0
****
n.s.
n.s.
TdLN
NdLN
SIINFEKL: H-2Kᵇ
Anti-TCR Vα2
BSA control

**Figure 6**

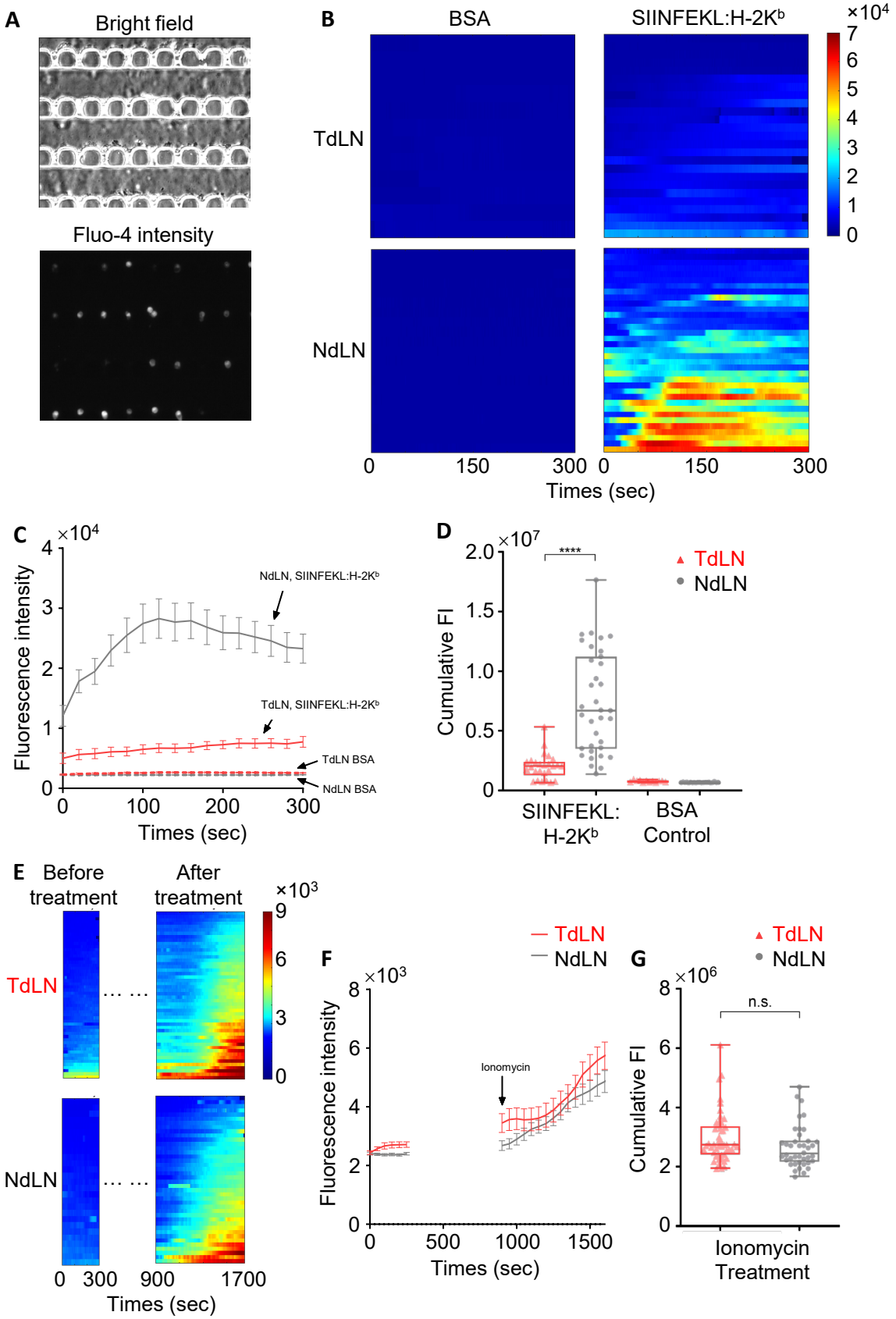
A
Bright field
Fluo-4 intensity
B
BSA
SIINFEKL:H-2Kᵇ
×10⁴
TdLN
NdLN
0
150
300
Times (sec)
C
×10⁴
Fluorescence intensity
NdLN, SIINFEKL:H-2Kᵇ
TdLN, SIINFEKL:H-2Kᵇ
TdLN BSA
NdLN BSA
Times (sec)
D
×10⁷
Cumulative FI
****
TdLN
NdLN
SIINFEKL: H-2Kᵇ
BSA Control
E
Before treatment
After treatment
×10³
TdLN
NdLN
0
300
900
1700
Times (sec)
F
×10³
Fluorescence intensity
Ionomycin
Times (sec)
G
×10⁶
Cumulative FI
n.s.
Ionomycin Treatment

**Figure 7**

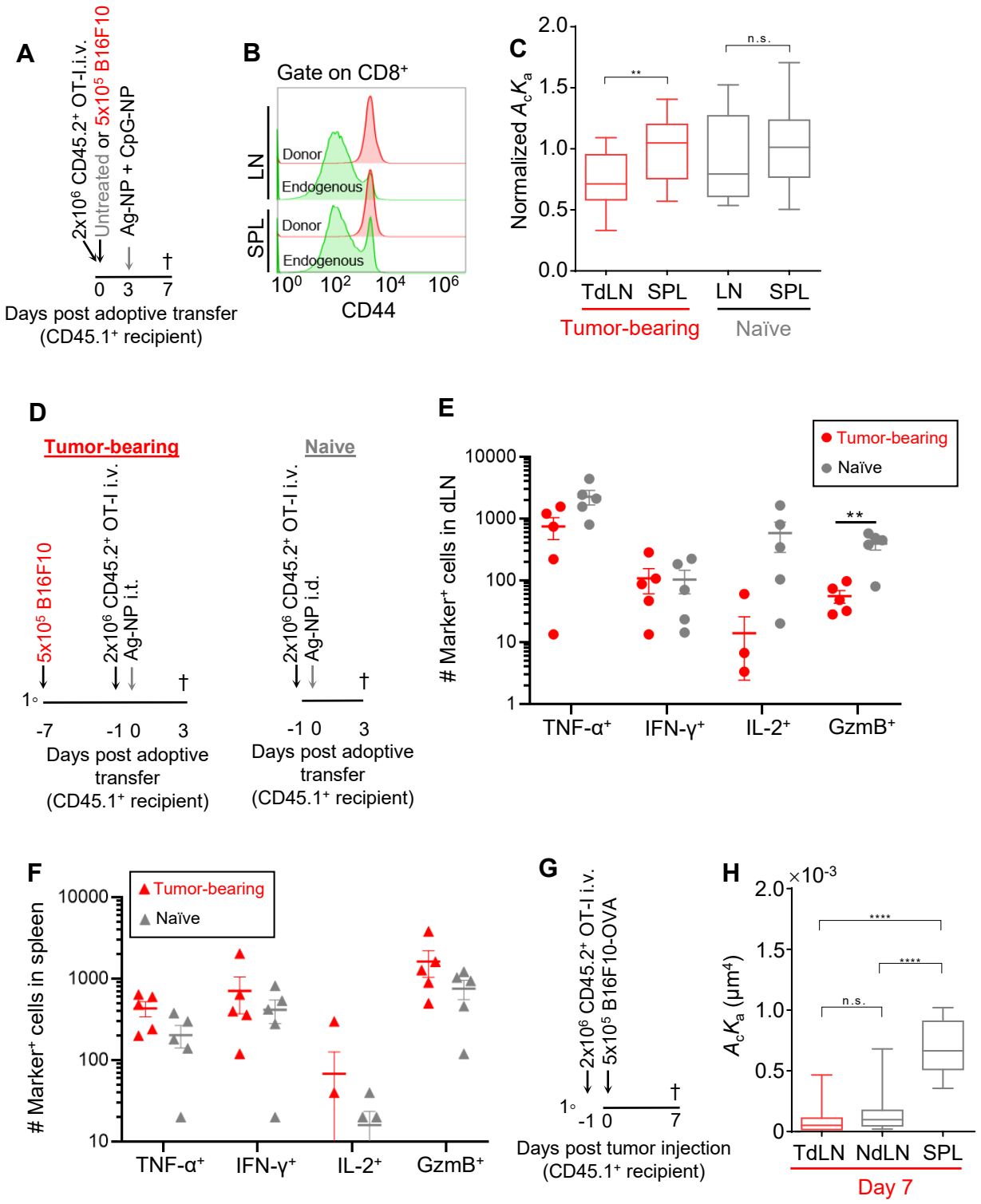
A
2x10⁶ CD45.2⁺ OT-I i.v.
Untreated or 5x10⁵ B16F10
Ag-NP + CpG-NP
0 3 7
Days post adoptive transfer
(CD45.1⁺ recipient)
B
Gate on CD8⁺
LN
SPL
Donor
Endogenous
CD44
C
Normalized AcKa
TdLN SPL LN SPL
Tumor-bearing
Naïve
n.s.
D
Tumor-bearing
Naive
5x10⁵ B16F10
2x10⁶ CD45.2⁺ OT-I i.v.
Ag-NP i.t.
Ag-NP i.d.
-7 -1 0 3
Days post adoptive transfer
(CD45.1⁺ recipient)
E
Tumor-bearing
Naïve
# Marker⁺ cells in dLN
TNF-α⁺ IFN-γ⁺ IL-2⁺ GzmB⁺
F
# Marker⁺ cells in spleen
G
2x10⁶ CD45.2⁺ OT-I i.v.
5x10⁵ B16F10-OVA
-1 0 7
Days post tumor injection
(CD45.1⁺ recipient)
H
AcKa (μm⁴)
TdLN NdLN SPL
Day 7

**Supplemental Figure 1**

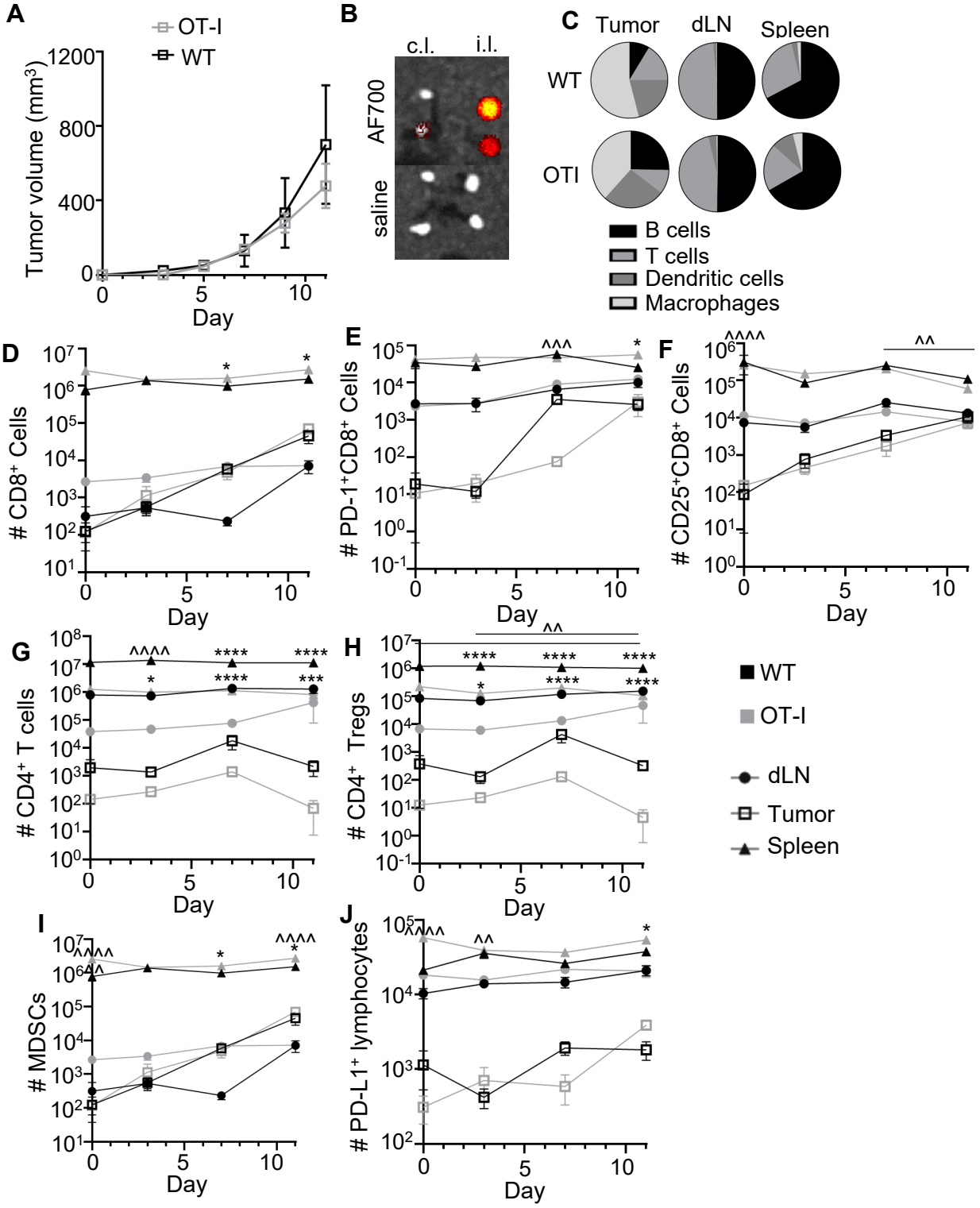
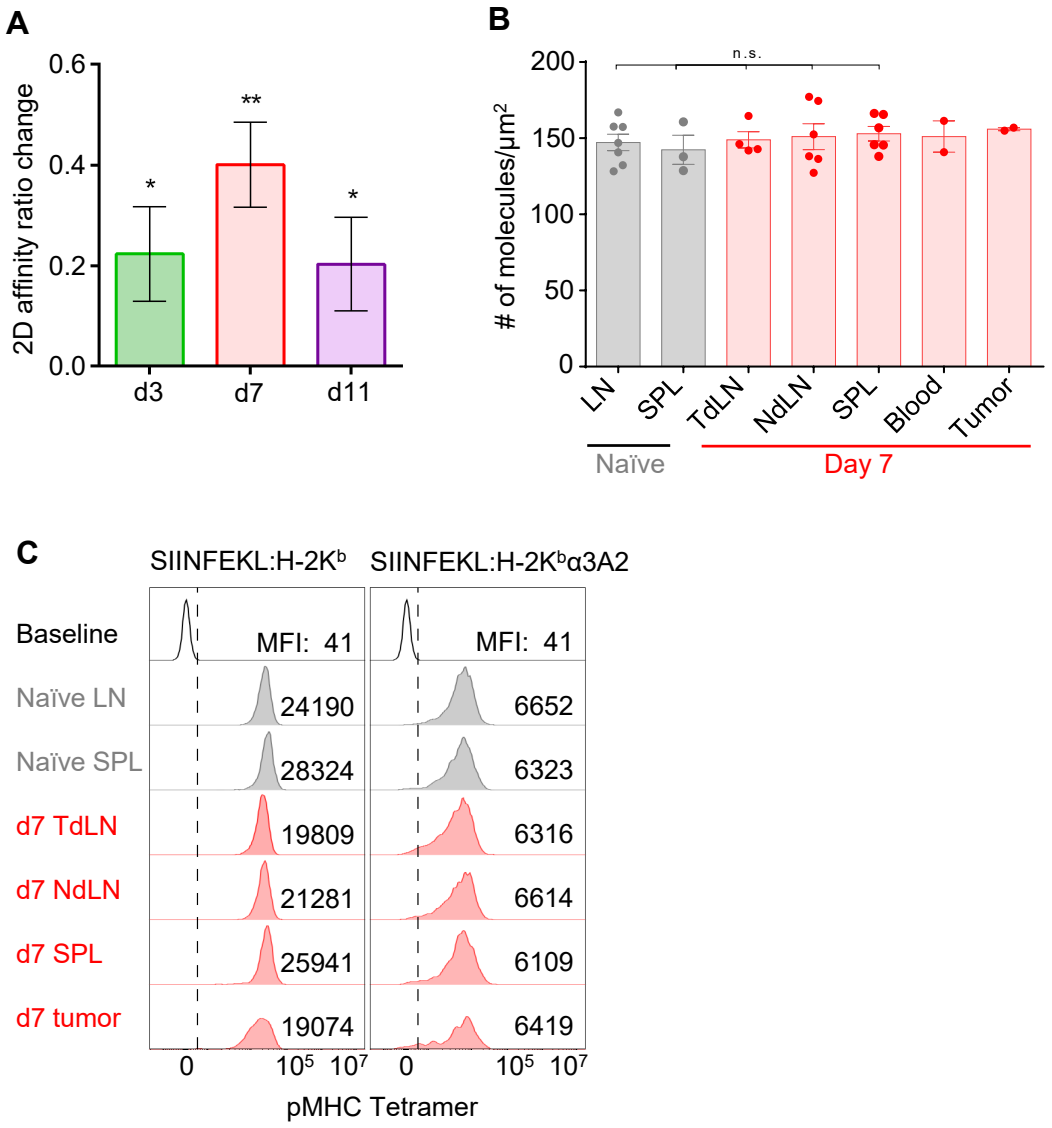
**Supplemental Figure 2**